

# Small Scale Systems of Galaxies. III.

## X-ray detected E+S galaxy pairs in low density environments

R. Grützbauch<sup>1</sup>, G. Trinchieri<sup>2</sup>, R. Rampazzo<sup>3</sup>, E.V. Held<sup>3</sup>

L. Rizzi<sup>4</sup>, J.W. Sulentic<sup>5</sup> and W.W. Zeilinger<sup>1</sup>

<sup>1</sup> *Institut für Astronomie, Universität Wien, Türkenschanzstraße 17, A-1180 Wien, Austria*

<sup>2</sup> *INAF - Osservatorio Astronomico di Brera, Via Brera 28, I-20121, Milano, Italy*

<sup>3</sup> *INAF - Osservatorio Astronomico di Padova, Vicolo dell'Osservatorio 5, I-35122, Padova, Italy*

<sup>4</sup> *Institut for Astronomy, University of Hawaii, Woodlawn Drive, Honolulu, HI 96822, USA*

<sup>5</sup> *Department of Physics and Astronomy, University of Alabama, Tuscaloosa, AL 35487, USA*

<sup>1</sup>gruetzbauch@astro.univie.ac.at, <sup>2</sup> ginevra@brera.mi.astro.it,

<sup>3</sup> roberto.rampazzo@oapd.inaf.it, <sup>3</sup> enrico.held@oapd.inaf.it, <sup>4</sup> rizzi@ifa.hawaii.edu

<sup>5</sup> giacomo@merlot.astr.ua.edu, <sup>1</sup> zeilinger@astro.univie.ac.at

### ABSTRACT

We present a comprehensive study of the local environments of four E+S galaxy pairs with the main goal to investigate their formation/evolution histories.

We obtained new XMM-Newton data for two pairs (RR 143 and RR 242) that complements existing ROSAT data for the other two (RR 210 and RR 216). The new observations reveal diffuse X-ray emission in both pairs with luminosities of  $L_X \sim 3 \times 10^{41}$  erg s<sup>-1</sup> (0.5-2.0 keV). The emission is asymmetric in both cases and extends out to  $\sim 500''$  (120 kpc) and  $700''$  (160 kpc) in RR 143 and RR 242 respectively. The nucleus of RR 242 hosts a low luminosity ( $L_X \sim 10^{41}$  erg s<sup>-1</sup>, 2.0-10 keV) mildly absorbed ( $N_H \sim 10^{22}$  cm<sup>-2</sup>) AGN. We find that the early-type components of pairs with diffuse hot gas appear to be relaxed objects while those in RR 210 and RR 216, where no diffuse emission has been found, display unambiguous signatures of ongoing interaction.

New wide-field V and R-band observations are used to study the photometric properties of the early-type components and to search for *candidate* faint galaxy populations around each of the pairs. While no diffuse optical light is found for any of the pairs, all of the early-type members show very extended and concentric luminous envelopes. We identify a faint galaxy sample in each field and we consider whether they could be physically associated with the luminous pairs based upon ( $V - R$ ) colors and photometric properties. We find that the distribution of  $r_e$  and  $M_R$  for the *candidates* are similar in three of the fields (RR 143, 216 and 242). The same selection criteria applied to the field of RR 210 suggest a fainter and more compact population possibly suggesting a larger background fraction than in the other fields.

*Subject headings:* galaxies: evolution — galaxies: individual (NGC 2305/2307, NGC 4105/4106, IC 3290/NGC 4373, NGC 5090/5091)

### 1. Introduction

High-redshift studies reveal the existence of a class of objects with structural, dynamical and stellar population properties very similar to those of normal nearby early-type galaxies (ETGs) ((see

e.g. Franx et al. 2003; Chapman et al. 2004; Treu et al. 2005). If ETGs are indeed the most evolved systems then these high redshift examples presumably suggest a quasi-primordial nature for ETGs implicit in the tightness of the fundamental scaling relations. At the same time, a large

amount of observational work indicates that a relatively large fraction of ETGs show evidence of interactions, accretions/mergers and recent star formation episodes. This suggests that predictions of  $\Lambda$ CDM hierarchical models for ETG formation cannot be ruled out (see e.g. De Lucia et al. 2006) even at low redshift.

Another open question involving ETGs is connected with the possible dissimilar evolution of these galaxies in different environments expected from hierarchical models. Hierarchical galaxy evolution is assumed to be ongoing with signatures of galaxy reprocessing possibly more evident in low density environments (LDEs). Peculiar morphologies (see e.g. Reduzzi et al. 1996; Colbert et al. 2001; Sulentic et al. 2006) and kinematical decoupling (see e.g. Falcon-Barroso et al. 2005) are indeed present in a significant fraction of ETGs in LDEs. Recent studies of line-strength indices identify signatures of very recent rejuvenation episodes in ETGs located in LDEs and, although there is a large spread in age, on average these ETGs are about 1.5-2 Gyr younger than their cluster counterparts (see e.g. Thomas et al. 2005; Annibali et al. 2006; Clemens et al. 2006).

The evolution of local ETGs in LDEs is also the subject of intense study in the X-ray domain. Chandra and XMM-Newton observations are clarifying the X-ray properties of loose groups of galaxies which are the defining aggregates in LDEs. A hot Intra-Group Medium (IGM) is detected primarily in loose groups containing an ETG population (see e.g. Mulchaey 2000). Early work (Zabludoff 1999) suggested that groups might fall into different classes defined by their X-ray properties: from groups with a luminous, extended, hot IGM centered on a giant E to groups with little or no diffuse emission. Several examples of these classes can now be found in the literature (see e.g. Mulchaey et al. 2003; Trinchieri et al. 2003; Belsole et al. 2003; Ota et al. 2004). In a hierarchical evolutionary scenario the final product of a merged group is expected to be an isolated luminous elliptical with extended X-ray halo and a few have been identified (see e.g. Mulchaey & Zabludoff 1999; Vikhlinin et al. 1999; Jones et al. 2003; Khosroshahi et al. 2004). At the same time, recent XMM-Newton observations of optically selected merger remnants like NGC 3921, NGC 7252 and Arp 227 (Nolan et al. 2004; Rampazzo et al.

2006) show that the hot gas is X-ray underluminous compared with mature E galaxies into which these merger remnants are expected to evolve (see also Sansom et al. 2000).

Both optical and X-ray observations offer possible evidence for *secular evolution* in LDEs. Indeed galaxy-galaxy tidal encounters (and mergers) should be more efficient in groups than in clusters because the velocity dispersion of a group is similar to that of an individual galaxy. Our goal is to extend optical and X-ray studies to physically isolated pairs of galaxies which are the simplest and most common aggregates in LDEs where we can study the evolutionary effects of galaxy-galaxy encounters at the “cellular level”. Mixed E+S binary systems are particularly interesting in the context of an evolutionary accretion scenario (see e.g. Rampazzo & Sulentic 1992; Hernandez-Toledo et al. 2001; Domingue et al. 2005). Optical and MIR studies provide evidence that the gas-rich spiral component may cross-fuel the elliptical component (Domingue et al. 2003) in some cases indicating a special mechanism for ETG secular evolution. Study of such relatively simple structures may shed light on a *possible evolutionary link* between poor groups and isolated Es. We have presently only very limited information on the X-ray properties of mixed pairs (Rampazzo et al. 1998; Henriksen & Cousineau 1999; Trinchieri & Rampazzo 2001) with detected ETG members showing X-ray luminosities and  $L_X/L_B$  ratios that span the full range observed for early-type galaxies in general. A group-like extension has been detected in some pairs but there is no evidence that pair membership affects the global X-ray properties of galaxies (Trinchieri & Rampazzo 2001). Detection of diffuse X-ray emission in some pairs might offer the best means to identify systems that are actively involved in a hierarchical merging process.

In the above context we present: 1) new XMM-Newton observations of two E+S pairs (RR 143 and RR 242) both of which show diffuse emission (plus pairs RR 210 and RR 216 previously observed with ROSAT (Trinchieri & Rampazzo 2001)) and 2) results of an optical photometric search for tidal features/optical diffuse light and a study of *candidate* faint galaxy populations that might be associated with the pairs. Groups studied by Zabludoff & Mulchaey (1998) revealed a

significantly higher number of faint galaxies ( $\approx 50$  members down to magnitudes as faint as  $M_B \approx -14 + 5 \log_{10} h_{100}$ ) in groups with a hot IGM compared to groups without this component. Section 2 of this paper reviews the presently known properties of our sample of pairs. Sections 3 and 4 describe the X-ray and optical observations as well as data reduction techniques. Individual results are presented in Section 5 while Section 6 presents an analysis of the properties of candidate faint galaxy members. A discussion of the results in the light of current literature is given in Section 7. We use  $H_0 = 75 \text{ km s}^{-1} \text{ Mpc}^{-1}$  throughout the paper.

## 2. The picture so far

The E+S pairs in our sample were taken from the Reduzzi & Rampazzo (1995) catalogue of isolated pairs in the Southern Hemisphere. Table 1 summarizes photometric, structural and kinematical properties of pair members extracted from the literature.

**RR 143** (NGC 2305 + NGC 2307) involves a very isolated pair with projected component separation  $R \approx 51 \text{ kpc}$  and velocity difference  $\Delta V \approx 270 \text{ km s}^{-1}$ . The much larger velocity difference implied by NED derives from an older and less accurate measurement for NGC 2307 (see Table 1). A study of the ellipticity profile for NGC 2305 (Reduzzi & Rampazzo (1996)) shows that the outer regions of the galaxy ( $r \geq 20''$ ) are on average flatter ( $\epsilon \approx 0.3$ ) than the inner ones ( $\epsilon \approx 0.22-0.25$ ) consistent with the presence of sub-structure. Isophotal shape analysis also supports the presence of sub-structure being boxy within  $20''$  of the center and disk between 20 and  $35''$ . A recent bulge/disk decomposition study (De Souza et al. 2004) suggests that the galaxy is lenticular rather than an elliptical. Kinematical studies however show that the galaxy has a maximum rotation velocity  $\leq 50 \text{ km s}^{-1}$  (Rampazzo 1988) which is more typical of an E than an S0.

**RR 210** (NGC 4105 + NGC 4106) form a strongly interacting pair (Arp & Madore 1987) separated by projected  $7.7 \text{ kpc}$  and  $258 \text{ km s}^{-1}$ . It can also be described as a loose triplet (Tully 1988) if one includes IC 764 with a similar recession velocity ( $2127 \text{ km s}^{-1}$ ) and a projected separation of  $46.3'$  ( $\approx 363 \text{ kpc}$ ). Reduzzi & Rampazzo (1996) obtained B, V and R surface photometry

for both components which show almost constant color profiles ( $B - V \approx 0.9-1$ ) suggesting that both are early-type galaxies. NGC 4105 shows no evidence of perturbation while NGC 4106 is strongly perturbed with arms/tails that are likely a product of interaction with the companion. NGC 4105 shows evidence for a dusty center and disk outer structure. NGC 4106 shows a disk central structure.

Longhetti et al. (1998a,b) obtained kinematic and spectro-photometric properties for both pair members. Evidence for strong interaction also comes from velocity and velocity dispersion profiles along a line connecting the nuclei of the two galaxies. Study of line-strength indices (Longhetti et al. 1999) suggests the presence of very recent star formation episodes. In particular NGC 4106 shows a value for the H+K(CaII) index larger than 1.3, i.e. larger than the maximum value attainable in post-starburst models (both with solar and super-solar metallicity) which suggests the presence of H $\epsilon$  in emission. This feature is considered a good indicator of recent star formation (Rose 1984, 1985). The detection of [OII] $\lambda 3727-9\text{\AA}$  emission in the nucleus of NGC 4105 is also suggestive of a recent star formation episode (Longhetti et al. 1998a).

Caon et al. (2000) showed the extended nature of the ionized gas distribution while mapping H $\alpha$  kinematics in NGC 4105. The ionized gas counterrotates relative to the stars and shows a different behaviour on opposite sides of the slit (P.A.  $151^\circ$ ) centred on the nucleus: the NW side shows a less steep central gradient, and a dip at about  $13''$ . This data points toward a past cross-fuelling or accretion event. The stellar velocity dispersion is quite high in both galaxies (see Table 1). NGC 4105 shows slow stellar rotation ( $(36 \pm 7 \text{ km s}^{-1})$  Caon et al. 2000) in contrast to the ionized gas rotation which reaches  $240 \pm 20 \text{ km s}^{-1}$ . Longhetti et al. (1998b) report a higher stellar rotation velocity  $\approx 116 \text{ km s}^{-1}$  for NGC 4106. Modeling of kinematics and surface photometry in NGC 4105 (Samurović & Danziger 2005) do not support the presence of significant dark matter at least inside  $\approx 1 r_e$ . Their models neglect any interaction with NGC 4106.

**RR 216** (IC 3290 and NGC 4373) form an isolated pair according to both Sadler & Sharp (1984) and Arp & Madore (1987) with a projected separa-

tion of 26 kpc and  $\Delta V = 54 \text{ km s}^{-1}$ . The system is in the Hydra-Centaurus region but located on the outskirts at  $4.9^\circ$  from the cluster center (Dickens et al. 1986). B, V, and R surface photometry (Reduzzi & Rampazzo 1996) shows  $(B - V) \approx 1$  throughout both galaxies although IC 3290 shows a well developed bar and a “grand design” spiral pattern. NGC 4373 shows disk structure in the isophotal shape profile but the luminosity profile is well represented by a  $r^{1/4}$  law suggesting that the galaxy is a disk E.

**RR 242** (NGC 5090 and NGC 5091) has parameters similar to the other pairs ( $R = 17 \text{ kpc}$ ,  $\Delta V = 108 \text{ km s}^{-1}$ ), but it is found in a richer local environment than the previous systems. Available NED data suggest that the pair is part of a loose group. Four additional luminous galaxies with comparable redshifts can be found within a radius of 300 kpc around NGC 4105: NGC 5082 (at  $5.8' / 77.5 \text{ kpc}$ ,  $\Delta V_{pair} = 421 \text{ km s}^{-1}$ ), NGC 5090A (at  $20.3' / 298.4 \text{ kpc}$ ,  $\Delta V_{pair} = 45 \text{ km s}^{-1}$ ), NGC 5090B (at  $13.8' / 184.1 \text{ kpc}$ ,  $\Delta V_{pair} = 773 \text{ km s}^{-1}$ ) and ESO 270 G007 (at  $24.4' / 326.1 \text{ kpc}$ ,  $\Delta V_{pair} = 275 \text{ km s}^{-1}$ ). If all above galaxies belong to a group, then it has an average recession velocity of  $3681 \text{ km s}^{-1}$  and a velocity dispersion of  $327 \text{ km s}^{-1}$ .

NGC 5090 appears to be a “bona fide” elliptical without signatures of interaction according to the surface photometry of Govoni et al. (2000). The galaxy hosts an FRI radio source (PKS B1318-434) with two jets aligned perpendicular to a line connecting the galaxy nuclei (see e.g. Lloyd et al. 1996, and references therein). Carollo et al. (1993) have obtained the velocity dispersion and rotation velocity profiles of NGC 5090 which show high central velocity dispersion and low rotation velocity, both characteristic of E galaxies. Bettoni et al. (2003) estimate a BH mass of  $1.1 \times 10^9 M_\odot$  for NGC 5090.

The X-ray picture given by *ROSAT* (Trinchieri & Rampazzo 2001) indicates that X-ray luminosities and  $L_X/L_B$  ratios of pairs encompass a very wide range, in spite of the very small number of objects studied. In particular, the 4 systems presented here have very different luminosities and X-ray morphologies in contrast to their relatively similar optical ones (see Table 1). In RR 143 and RR 242 the X-ray emission is much more extended than the optical light. It can be rea-

sonably interpreted as associated with a “group-type” potential. Relatively faint and compact emission (i.e. within the optical galaxies) is detected in RR 210 and RR 216. Although no spectral properties could be derived from the ROSAT-HRI data, the observed luminosities would point to emission from the galaxy only, possibly from the evolved stellar population, with little/no contribution from a group component.

### 3. Observations and Reduction

#### 3.1. X-ray XMM-Newton observations

We obtained XMM-Newton observations of RR 143 and RR 242 with EPIC in the Medium filter as reported in Table 2. We used the XMM-Newton Science Analysis System (SAS) version *xmmsas\_20050815\_1803-6.5.0* to clean the data from flaring events (which reduced the original exposure by  $> 30\%$ : see Table 2) and to filter them with the standard “FLAGS” (see the science threads at <http://xmm.vilspa.esa.es>). We retain single, double and quadruple events for morphological and MOS spectral analysis. We consider only single events for spectral analysis of the PN data. We also made use of both *CIAO*<sup>1</sup> and *DS9/Ftools*<sup>2</sup>. CCD gaps are masked out during the spatial analysis. In order to improve statistics and to avoid having to take into account the different CCD gap patterns of the two instruments, we summed all EPIC-MOS data and kept the EPIC-PN data separate. These two datasets will be used for all except the spectral analysis in this work.

##### 3.1.1. Source extent

We smoothed the EPIC-MOS data with an adaptive filter in order to better visualize the emission. We show 0.5-2.0 keV isointensity contours superposed on our optical images (see Section 3.2) in Figure 1. The extended emission is centered on the brighter early-type component (NGC 2305 in RR 143 and NGC 5090 in RR 242) in both pairs. The spiral galaxies (NGC 2307) in RR 143 and NGC 5082 west of RR 242 also detected as discrete sources. A number of additional sources are seen in both fields of the pairs. However in all but

<sup>1</sup><http://cxc.harvard.edu/ciao/>

<sup>2</sup><http://head-cfa.harvard.edu/RD>

one case (Galaxy # 13627 in RR 242, Table 8. coincident with the X-ray source #23 in Table 10), the X-ray sources are most likely background objects unrelated to the pairs. We present them in the Appendix and in Tables 9 and 10 for completeness, but we will not use them in the present discussion.

We employed azimuthal averaging to assess the extent of the diffuse emission in different energy bands. This is only an approximation, because the emission is not azimuthally symmetric around either pair. This approximation allows us to measure a total average extent and to determine the background level. We excluded discrete sources from the profiles which are all centered on the early-type components.

Evaluation of the background for extended sources is always a challenge, as shown by several authors (see Nevalainen et al. 2005; Read & Ponman 2003) and notes to the use of *xmmsas* software. Background maps can be obtained as a byproduct of the detection procedure in the *xmmsas* software. A central extended source is not excised, however, since the program is designed to also provide a correct background for sources embedded in diffuse emission. Blank sky fields are available at <http://xmm.vilspa.esa.es/> and can be used to determine the background. They are unfortunately based on thin filter data while ours are medium filter observations. We therefore analyzed several images, both from the archive and from our own data, to evaluate the shape of the background with the medium filter. A comparison with the thin filter data indicates no significant differences, except for a different relative normalization for profiles obtained in different energy bands. We have therefore evaluated the background from the deep field blank sky data, and normalized them to our own fields in the outer regions, where the radial profiles show an almost constant surface brightness, very similar in shape to that of the background fields. The results for RR 143 are given in Figure 2 as an example. The same figure also shows that the emission is prominent in the 0.5-2.0 keV profile and becomes negligible above 3.0 keV. Since the contribution in the 2-3 keV range is not significant, and it is confined to the inner regions, we have used the 0.5-2.0 keV data to study the radial distribution of the emission. The same considerations apply to

RR 242.

Figures 3 and 4 show the net, azimuthally averaged profiles from PN and MOS data separately. Emission in RR 143 extends to almost 500'' radius ( $\sim 120$  kpc). The profile of RR 242 shows a very prominent central source that dominates emission in the inner  $\sim 1'$  region. A more extended component extends to  $r \sim 700''$  (160 kpc). X-ray contours in RR 143 show that the emission is far from azimuthally symmetric. We produced radial profiles at different position angles in order to quantify the degree of asymmetry. We find that the asymmetry is also a function of radial distance from the center. This motivated us to divide the emission into different azimuthal and radial zones (Figure 3 central and right panels). Figure 3 confirms significant azimuthal differences in the data which confirm visual impressions taken from the iso-intensity contours. Asymmetries are also visible in the X-ray emission from NGC 5082 which is an SB(r)0 member of the RR 242 system. In Figure 5 we show the comparison of radial profiles obtained in different quadrants to illustrate the evidence for azimuthal asymmetry. The photon distribution is clearly compressed to the SE, while the NW quadrant appears more extended.

### 3.1.2. Spectral analysis

In order to measure the spectral properties of the X-ray emission we extracted photons from different regions, including background regions appropriate for the emission region we want to investigate. Given the pattern in the PN detectors, regions in MOS and PN are often not the same. The central region is typically the same because it fits on the same CCD on PN. The more extended emission is taken from MOS while PN is limited to the region that fits on a single CCD. For this reason the relative normalization between instruments is left free to vary in order to compensate for the different regions considered.

We used a local determination of the background, when possible, from an annulus around the region considered (in general this is true for the MOS1 and MOS2 data sets, and for the central source in the PN data). This also implies that the surrounding “galaxy” is used as background for the central source in RR 242. For PN, the background is taken from a region free of source emission and also free of gaps close to the region of

interest. Since the emission from the source does not fill the whole field of view in either galaxy, and the background level where the source ends is not significantly reduced relative to the central parts we have used a local determination also for the whole source; this reduces uncertainties due to the background variations between different observations, unavoidable when using a different set of data (like the blank fields, that we cannot use in any case due to the different filters).

The data are binned to increase the statistics. We have considered binning to a specific number of photons, which is reasonable for some regions. However, since the contribution of the background is not uniform with energy, and is larger at high energies, we have also considered larger bins mostly at high energies to increase the signal-to-noise of the net emission in each bin. In all cases we have considered only bins that have a S/N of at least  $2\sigma$  after background subtraction. The data are fitted in XSPEC with either a plasma (namely MEKAL in the XSPEC acronyms) or a combination of plasma and bremsstrahlung or power law to account for high energy tails. Low energy absorption is also taken into account and abundances are according to Wilms et al. (2000). The results are given in Table 3 and discussed later for each source.

## 4. Optical wide-field observations

### 4.1. Observations

CCD imaging of all 4 galaxy pairs and their surrounding fields was obtained with the ESO 2.2m telescope using the Wide Field Imager (WFI). The mosaic is composed of 8 EEV “CCD 44” type CCDs, each having  $2048 \times 4096$  pixels. The pixel scale is  $0''.238 \text{ pixel}^{-1}$  yielding a field-of-view of  $34 \times 33 \text{ arcmin}^2$ . A single field centered on each galaxy pair was observed in Service Mode between Nov. 2001 and June 2004. Each field was observed in the Johnson-Bessell *V* and *R* bands (ESO filters *V*/89–ESO843 and *R*<sub>c</sub>/162–ESO844) with total exposure times of 3000 s in both filters (see the Observing Log in Table 4). The observing conditions were generally photometric. Standard stars from Landolt (1992) were also observed each night in one or two reference CCDs. In order to fill the gaps between the CCDs, as well as to remove bad columns and cosmic ray hits, multiple 500 s images

were recorded for each field. To this purpose, the images were suitably dithered in all cases except one (RR 143).

### 4.2. Reduction and calibration

Reduction of the CCD mosaic data was accomplished with IRAF<sup>1</sup> using standard procedures. All multi-extension images were bias-subtracted and divided by twilight flat fields using the Mosaic reduction package `mscred` (Valdes 1998). Images were then astrometrically calibrated and registered onto a common distortion-free coordinate grid using `mscred` and the pipeline script package `wfpred` developed by two of us at Padua Observatory. Astrometric calibration was done using the USNO Catalogue (Zacharias et al. 2000). The internal (image-to-image) astrometric precision is on the order 0.1 arcsec while the systematic error of object coordinates is  $\sim 0.2 - 0.3$  reflecting the intrinsic accuracy of the USNO Catalogue.

Before co-addition all CCD images had their counts rescaled (“normalized”) to match the photometric zero point of a reference CCD. We adopted CCD#2 as our reference frame and used the relative zero points of the eight CCDs determined by Rizzi (2003). All CCDs, once referred to a common zero point, were combined into a single  $8000 \times 8000$  image in each band/exposure. All exposures were finally registered and median-combined to create a final image for each target, which covers an area of approximately  $32' \times 32'$ . In these images all CCD blemishes and gaps are canceled out, except for RR 143. Figures 7, 8, 9 and 10 show the regions of the sky covered by the frames of RR 143, RR 210, RR 216 and RR 242, respectively.

Since the images in each dataset (Observing Block) were taken consecutively under photometric sky conditions the median-combined images were calibrated by adopting the average airmass of each observation (see Table 4). Photometric calibration was accomplished separately for each dataset using standard stars obtained on the same nights in order to monitor the nightly zero point variation using the reference CCD#2. A set of

<sup>1</sup>IRAF is distributed by the National Optical Astronomy Observatories, which are operated by the Association of Universities for Research in Astronomy, Inc., under cooperative agreement with the National Science Foundation.

linear calibration relations was then computed for each night:

$$V = v' + a_V(V - R) + zp_V \quad (1)$$

$$R = r' + a_R(V - R) + zp_R \quad (2)$$

where  $v'$  and  $r'$  are the instrumental magnitudes normalized to 1 s exposure and corrected for atmospheric extinction. The following extinction coefficients were adopted:  $k_V = 0.12$ ,  $k_R = 0.09$ . The adopted color terms of the calibration were  $a_V = -0.140 \pm 0.013$  and  $a_R = -0.004 \pm 0.016$ , while the zero points are those given in the last column of Table 4. The zero point uncertainties of the calibration relation are of the order 0.03 mag in both  $V$  and  $R$ . These relations were used to calibrate the instrumental magnitudes in our photometric catalogs of the target fields (see Sect. 3.4).

### 4.3. Surface photometry of bright pair members

Surface photometry of the bright pair members was carried out with the ellipse fitting routine in the STSDAS package of IRAF and with the GALFIT package (Peng et al. 2002). While the ELLIPSE task computes a Fourier expansion for each successive isophote (Jedrzejewski 1987), resulting in the surface photometric profiles shown in Figure 11, GALFIT was used to perform a bulge-disk decomposition – if needed – and to determine the parameters of a Sersic model fit to the galaxies bulge component. The Sersic profile is a generalization of the de Vaucouleur’s law with  $\mu(r) \sim r^{1/n}$ , where the Sersic parameter  $n$  is a free parameter (Sersic 1968). This profile is thus sensitive to structural differences between different kinds of ETGs providing a better fit to real galaxy profiles.

Two methods were used to search for fine structure and signatures of interaction. 1) A model of the ETG in each pair was derived from the ELLIPSE output and subtracted from the original image. 2) The image was convolved with an elliptical Gaussian function yielding an unsharpened version of the image which was then subtracted from the original image.

### 4.4. Detection of diffuse light around bright galaxies

A search for optical diffuse light around the early-type components was carried out with the SourceExtractor (see also next section). All sources detected as “object” were masked yielding a background-only image where large-scale diffuse light might best be detected. This procedure is very sensitive to errors in the background determination which, in our case, are caused by the gaps between individual CCDs (for RR 143) or the presence of bright foreground stars (for RR 242).

A large extent for all of the systems is measured from our data - a useful number in this context is the surface brightness of the last detected isophote of the ETG and its semi-major axis. These values (in the R band) are  $25.45 \pm 0.01$  mag arcsec<sup>-2</sup> at 64 kpc (RR 143),  $25.48 \pm 0.01$  mag arcsec<sup>-2</sup> at 38 kpc (RR 210),  $26.39 \pm 0.02$  mag arcsec<sup>-2</sup> at 137 kpc (RR 216) and  $24.85 \pm 0.01$  mag arcsec<sup>-2</sup> at 65 kpc (RR 242). The typical background fluctuations were used to estimate upper limits above which diffuse light becomes undetectable in our R band images. The background level was estimated in 10 squares of  $20 \times 20$  pixel across the images. This procedure yielded RMS values of  $\sim 0.3\%$  -  $1\%$  for the different fields. From these values we determined the following limits in mag arcsec<sup>-2</sup> for the 4 frames: 25.8 for RR 143, 25.4 for RR 210, 26.5 for RR 216 and 25.9 for RR 242. We found no evidence for extended diffuse light although filamentary structure was detected in RR 216 (Figure 12). To quantify the significance of this detection we compared the typical background fluctuation in this field (see above) with the excess light of the plume. The detection limit for this field was determined to be in the order of 0.3%, while the intensity of the plume exceeds the mean background value by  $\sim 3\%$  corresponding to a surface brightness of  $\sim 24$  mag/arcsec<sup>2</sup>.

To compare our results with isolated ETGs we also examined  $40' \times 40'$  fields around the 4 ETGs using the POSS II digital R-band images. Low-pass median filtering of the images revealed in all cases the existence of a faint, spatially extended envelope which appears roughly symmetrical around the ETG. The largest envelope was found for the early type component in RR 216 with a diameter of about 120 kpc, supporting the

above measurements from the new WFI data. In this context it is interesting to note that two of the most isolated ETGs, with luminosity and distance comparable to our pairs, do not show such extended envelopes Verdes-Montenegro et al. (2005); Sulentic et al. (2006).

## 4.5. The candidate faint galaxy population

### 4.5.1. Detection and sample definition

A population of faint galaxies around each pair was identified from SExtractor (Bertin et al. 1996) processing of the WFI images. The search involved a  $0.5^\circ \times 0.5^\circ$  field centered on each pair. We adopted criteria similar to those applied in the search for faint galaxy populations in poor groups (Grützbauch et al. 2005a,b). The algorithm was used to detect extended sources, i.e. sources with a *stellarity* parameter  $\leq 0.5$  (Bertin et al. 1996). The sample was limited to candidates larger than  $a \geq 1.5''$  and brighter than  $R = 21$  mag.

The expected contribution from background galaxies was estimated using the program `GalaxyCount`<sup>2</sup> (see Ellis & Bland-Hawthorn 2006). The program calculates the number of background galaxies (and standard deviation) expected in a magnitude limited observation of a given field. This program was used to emulate the characteristics of our observations and the selection criteria used for galaxy identification with SExtractor. We adopted an average seeing  $0.8''$ , a search area  $A 33' \times 33'$ , and an exposure time  $t = 50$  minutes with the collecting area of a 2.2m telescope. We further adopt a throughput of 60% for the WFI instrument. Using a range of S/N values we derive for the interval  $15.0 < m_R < 19.5$  mag  $\approx 170\text{-}200 \pm 20$  galaxies with a completeness of about 95%. The numbers are compatible with the galaxies found in our field of view suggesting that we are exploring very low galaxy density regimes. Over-densities, due to galaxy structures, if any, are expected to be very small.

The color-magnitude diagrams of detected galaxies in the four respective fields are shown in Figure 13. Our sample galaxies follow the well known trend discussed in (see e.g. Faber 1973), where fainter objects have bluer colors, reflecting the expected lower metallicities of less massive

galaxies (Dressler 1984). This trend is well defined in the blue color regime while contamination with background objects becomes evident at the red end of the distribution. The bold line in Figure 13 represents the color-magnitude relation for the Virgo cluster (Visvanathan & Sandage 1977) adjusted for the respective pair recession velocities. A color restriction of  $\pm 0.5$  mag on either side of the relation, representing generous limits to the early-type sequence, is the most effective way to remove the majority of background objects (see e.g. Khosroshahi et al. 2004). Therefore, all objects with  $(V - R) > 1$  were excluded from the sample (dashed line), leading to the exclusion of 4 - 15 objects/system. The color-restricted candidate population of all groups then has a mean color of  $(V - R) = 0.58 \pm 0.17$  mag.

### 4.5.2. Surface photometry of candidate faint members

Surface photometry was performed on this sample using the `GALFIT` package. We used an automatic fit with a 1 component Sersic law ( $\mu(r) \sim r^{1/n}$ ) and obtained parameters such as central and effective surface brightness ( $\mu_0$  and  $\mu_e$  respectively), effective radius  $r_e$  and, of course, the Sersic parameter  $n$ . The resulting surface photometric properties of all four samples can be found in Tables 5 - 8. Figure 14 shows some examples of the surface photometry of faint candidate galaxies where the surface photometric profiles were obtained with the `IRAF-ELLIPSE` task and are compared to the `GALFIT` model (solid line in the surface brightness panel). The central area affected by the seeing (usually  $\sim 0.8''$ ) is not shown in the plots.

### 4.5.3. Projected spatial distribution of the faint candidate galaxy population

The spatial distribution of the faint candidate members was investigated by computing the local projected density around each object. This estimate is based on a method described by Dressler (1980). It consists of determining the radius - and the corresponding area in  $\text{Mpc}^2$  - within which the 10 nearest neighbors of each galaxy reside and hence computing the projected number density of galaxies  $\text{Mpc}^{-2}$  for each galaxy position. These values are then interpolated to a grid using the thin plate splines interpolation within

<sup>2</sup><http://www.aao.gov.au/astro/GalaxyCount/>



EasyMapping<sup>3</sup>. The resulting iso-density maps of the color-restricted candidate samples are shown in Figure 16 for each of the four systems of galaxies.

## 5. Results

### 5.1. The X-ray picture

X-ray maps of RR 143 and RR 242 reveal the presence of a diffuse intragroup medium in both systems. However, the spatial distribution of the X-ray photons from the two groups show some differences. X-ray emission from RR 143 extends out to  $r > 100$  kpc and its morphology is rather disturbed with an anisotropic distribution of photons that is not an artifact of the smoothing process. Figure 3 shows that the photon distribution is not the same at different position angles and radial distances. ROSAT-HRI data (Trinchieri & Rampazzo 2001) already revealed an elongated source associated with RR 143. One of the directions of elongation is toward the companion galaxy which could indicate a link/interaction artifact. However no optical evidence of tidally generated asymmetries has been detected in either galaxy. The bulk of the emission is centered on the early-type component although the late-type companion (NGC 2307) is also detected (source # 21 in Table 9). The energy distribution of photons from this galaxy (namely below and above 2 keV) suggests a mildly absorbed source, which would point toward a nuclear source as the origin of most of the X-ray emission with luminosity  $L_{(2.0-10.0)} \sim 3 \times 10^{40}$  erg s<sup>-1</sup>.

The spectral characteristics of the extended component can be modeled with a  $\sim 0.53$ keV plasma (0.52-0.56 at 90% confidence level,  $\chi^2_{\nu} \sim 1.4$ ). The addition of a power law or a bremsstrahlung model with fixed  $\Gamma = 1.5/kT=10$  keV gives a significant improvement ( $\Delta\chi^2 > 10$  with one additional parameter) and accounts for the excess above 2-3 keV. Figure 6 shows the data and best fit model using the data from all three instruments. We find no significant differences if we limit ourselves to the central 20'' radius or if we consider a larger area. In all cases we find a fea-

ture in the residuals around 1-1.5 keV that we are not able to model even taking into account variable abundances, multi-temperatures, and a cooling flow. All consistently yield temperatures around 0.5 keV (the cooling flow range is 0.3-0.8) and solar abundances. We find marginally improved results with a model where the abundance ratio between different elements is not fixed: i.e. with Fe overabundant and C under-abundant relative to the other elements. The residuals at 1-1.5 keV are somewhat smaller but are still present. Results are given in Figure 6 for the PN data alone. The absolute values of the abundances are not constrained so we put little weight on their relevance in the discussion. The total X-ray luminosity of the intragroup medium is  $L_X \sim 3 \times 10^{41}$  erg s<sup>-1</sup> (0.5-2.0 keV) with an average density of  $n_e \sim 8 \times 10^{-4}$  in the inner 200'' and a corresponding gas mass of  $8 \times 10^9 M_{\odot}$ .

The distribution of X-ray photons in RR 242 is more extended and less asymmetric than in RR 143. The source shows a prominent peak centered on the nucleus of RR 242a (NGC 5090) and consistent with the position of the radio source PKS B1318 -434 whose axis is oriented perpendicular to the line joining the pair components. This suggests that the tidal interaction may be influencing the way that the central engine of the elliptical is fueled.

The radial profile of the extended emission that is shown in Figure 4 can be modeled with two, or even three, components (right panel): at  $r < 30''$ , the emission is consistent with the instrumental PSF<sup>4</sup>. A significantly flatter component is present at  $r > 200''$  that can be modeled with a  $\beta$ -profile with a core radius  $r_c \sim 420''$  and  $\beta \sim 1$  (see figure). These two components do not completely describe the data: the central region appears more extended than a simple PSF. The addition of a  $\beta$ -profile with  $r_c \sim 45''$  and  $\beta \sim 1$  could account for the excess emission. This would imply that the central peak is due to both a nuclear component and a galactic component.

The spectral results for emission within a 30'' radius are consistent with the presence of a low luminosity ( $L_X \sim 10^{41}$  erg s<sup>-1</sup>, 2.0-10 keV) and

<sup>3</sup>EasyMapping is a mapping software developed by Olivier Monnereau and is available from <http://perso.wanadoo.fr/olivier.monnerau/EasyMapping.htm>

<sup>4</sup>We have used the analytical formula given by the "EPIC status of calibration and data analysis" document [XMM-SOC-CAL-TN-0018], of 11/02/05

mildly absorbed ( $N_H \sim 10^{22} \text{ cm}^{-2}$ ) AGN surrounded by emission from a moderately sub-solar 0.61 keV plasma. The luminosity of the latter component ( $L_x = 5 \sim 10^{40} \text{ erg s}^{-1}$ ) is consistent with emission from the ISM of the galaxy also taking into account a possible contribution from the surrounding IGM. The larger scale component is also consistent with emission from a hot plasma. The emission is best modelled using a two-temperature plasma ( $kT_1 \sim 0.3 \text{ keV}$  and  $kT_2 \sim 2.5 \text{ keV}$ ) both with approximately solar abundance. The total luminosity of the extended component is  $L_X(0.5-2.0) \sim 3 \times 10^{41} \text{ erg s}^{-1}$  and is dominated by the contribution from the hotter one (ratio about 10:1). The average density in the inner  $\sim 50 \text{ kpc}$  is  $n_e \sim 2$  and  $7 \times 10^{-4} \text{ cm}^{-3}$  for the softer and harder components respectively. This decreases to  $n_e \sim 0.9$  and  $2 \times 10^{-4} \text{ cm}^{-3}$  in the 50-100 kpc region.

The spiral companion is not detected with certainty as a discrete source; however, a source with  $ML \leq 10$  is found coincident with the position of the galaxy (with  $f_{0.5-2.0} \sim 2 \times 10^{-14} \text{ erg cm}^{-2} \text{ s}^{-1}$ , or  $L_x \sim 6 \times 10^{39} \text{ erg s}^{-1}$ ). This would be consistent with the expected luminosity of a normal spiral galaxy. Figure 1 shows a distortion in the iso-intensity contours at the position of the galaxy is visible in Figure 1 which also suggests some contribution from it. NGC 5082 located W of the pair is clearly detected as source # 8 in Table 10 with a 0.5-2.0 keV luminosity of  $\sim 8 \times 10^{40} \text{ erg s}^{-1}$ . The emission in the vicinity of NGC 5082 appears disturbed with indications of a tail towards the NW and of compression towards the SE. This can also be seen in Figure 5 at a distance of 20-50'' (5-13 kpc). This might indicate transverse motion of this galaxy relative to the group. Optical data do not show morphological asymmetries that might be a signature of ongoing interaction. At the same time the prominent bar in NGC 5082 could represent the signature of interaction involving the group members (Noguchi 1987).

## 5.2. Optical data

The WFI image of RR 143 is shown in Figure 7 together with a close-up of the pair after model subtraction of the ETG designed to reveal possible fine structure. Surface photometry of the ETG component RR 143a is shown in Figure 11 (top left). Unfortunately the non-dithered

frames for this object introduces large errors in the Fourier expansion especially from about 1.5' onwards. The isophotal ellipticity was fixed at  $\epsilon = 0.3$  in order to extend the fit despite the large area masked by the gaps. This may lead to an overestimation of the surface brightness at the outskirts of the galaxy with resultant overestimation of the structural parameter  $n$ . However the surface brightness profile shows evidence for a flat outer slope indicating large  $n$ . The model obtained with GALFIT gives  $n = 6.2$  with an effective radius of  $r_e \sim 50''$  (12 kpc). The boxiness of the inner isophotes noted by Reduzzi & Rampazzo (1996) can be confirmed out to  $\sim 20''$  (5 kpc) whereas the shape of the subsequent isophotes is certainly affected by the presence of a foreground star  $\sim 50''$  from the center of RR 143a. This star is also responsible for the bump in the  $(V - R)$  color profile as well as for the residuals in the model-subtracted image in Figure 7. A shell-like feature can be seen in the residual image while the unsharpened masked image shows no signatures of fine structure. We conclude that apart from a maximum 2% boxiness of the inner isophotes no fine structure is present in RR 143a.

Figure 8 shows the interacting pair RR 210 and its environment. Obvious interaction induced features are seen, especially in RR 210b. A Gaussian smoothed image reveals tidally disturbed arms, a possible bar-like structure and fine structure also in the ETG member RR 210a. The latter feature is probably caused by a dust-lane: Dust-filaments surround the core of RR 210a at a radius of  $\sim 15''$  (2 kpc) and extend out to  $\sim 30''$  (4 kpc) on the NW side. Other features in the model subtracted image are probably due to residuals or may belong to the highly perturbed RR 210b which can be argued to be in the foreground. No shell structure is detected in the ETG.

The surface brightness profile for RR 210a is not well fit with a single component model, most likely due to the presence of RR 210b. At  $\sim 40''$  (6 kpc) light contamination from the neighbor becomes dominant. We find no evidence for sub-structure in the regular extended halo surrounding the pair. Surface photometry of the elliptical RR 216b (Figure 11) reveals homogeneous profiles out to a radius of about 80'' (19 kpc) with: a) smoothly decreasing  $\mu$  and  $(V - R)$  color, b) slightly increasing  $\epsilon$  and c) constant position an-

gle and Fourier coefficients. In the galaxy’s outer parts ( $\sim 1.5'$ , 20 kpc) the surface brightness profile becomes very flat. It is best fit with a very high value of  $n = 8$  and an extended  $r_e = 150''$  (35 kpc). This flattening coincides with strong boxiness of the isophotes (more than 5%) and an increased ellipticity. This may argue for the presence of a second physically distinct component of diffuse stellar light surrounding the pair. However a large value of  $n$  is also needed to model the central part of RR 216b and the one component fit is a good representation of the surface brightness profile over  $\sim 8$  magnitudes.

Evidence for recent interaction is detected with the model subtracted image in Figure 9 revealing a ripple east of the center at a radius of about  $80''$  ( $\sim 20$  kpc) and an asymmetric excess of light along the major axis (North). One of the grand design spiral arms in RR 216a shows a sharp bend towards the elliptical. The homogeneous color profile throughout the pair (first reported by Reduzzi & Rampazzo (1996)) argues for RR 216a not being a true spiral but probably an ETG with tidally excited arms (tails).

The surface brightness profile of the bright elliptical RR 242a is well represented by a Sersic law with a high  $n = 7.5$  and a very extended  $r_e \sim 400''$  (98 kpc), a value typical for bright cluster ellipticals. Residuals of the one component fit point toward the presence of a second physically distinct component representing the outer extended halo of the galaxy. Of course the outer slope may be affected by a bright foreground star that can bias  $n$  towards a higher value. However the central part of RR 242a shows a luminosity excess, redder color and flattening of the profile towards the center (coinciding with a change in position angle). This is due to a circumnuclear disk of absorbing material that is also responsible for variations in the other profiles in the central part (within  $2\text{--}3''$  radius). The visible extension of the disk is  $\sim 2''$  (0.5 kpc). This nuclear disk has the same position angle as the spiral RR 242b which shows an asymmetric dust distribution in its disk with more absorbing material on the side towards RR 242a (see Figure 10, *bottom left*). We therefore argue that material transferred (cross-fuelled) from the spiral to the center of the elliptical is assembled in a central disk and may be responsible for fueling the AGN in RR 242a. No signature of fine struc-

ture was found. RR 242a appears to be an old and unperturbed system sharing some photometric characteristics with bright cluster ellipticals.

Diffuse light was detected only in RR 216 (Figure 12). An extended plume emerges towards the north side of the galaxy and curves towards the east/southeast represents reasonable evidence for ongoing interaction in this system. The plume is detected out to a radius of about  $4'$  (56 kpc) from the center of the ETG member and spans more than  $8'$  ( $\sim 110$  kpc) in projection. We could model the entire surface brightness profile of RR 210a with a high value of the Sersic parameter  $n = 6.5$  and  $r_e \sim 90''$  (13 kpc). The model does not match the luminosity profile at the center (see Figure 11). Moreover the outer halo has a slightly different isophotal ellipticity and position angle relative to the main body of the galaxy. Although such extended halos appear to be connected with the presence of diffuse light (see e.g. Gonzales et. al 2005) we did not detect such emission in our data.

## 6. Considerations on the faint candidate members in the four systems

In this section we present a comparative analysis of the photometric and structural properties of the faint galaxy populations that we identified on the basis of  $(V - R)$  color. We assume that these faint objects are at the same distances as the bright systems near which they are projected. Three of the pairs (but not RR 210) show very similar recession velocities (Table 1). Figure 15 shows the distribution of photometric parameters  $r_e$ ,  $n$  and  $M_R$  as determined from the fitting procedure described earlier. We selected 151, 172, 160 and 102 candidate galaxies in the RR 143, RR 210, RR 216 and RR 242 fields respectively. Figure 16 indicates that they have a smooth spatial distribution only for the RR 242 field. Both RR 210 and RR 216 show clumps of denser regions towards the NW of RR 210 and W of RR 216. The galaxy distribution in RR 143 is intermediate with less prominent concentrations towards the SW and NW.

Figure 15 shows that the Sersic index distribution peaks at  $n \sim 1$  consistent with the galaxies being either faint late-type or low-mass early-type dwarf galaxies (Binggeli, Sandage & Tarenghi 1984). The  $M_R$  distributions of these objects in

RR 143, RR 216 and RR 242 are very similar with peaks at  $M_R \sim -14.8$ ,  $M_R \sim -14.3$  and  $M_R \sim -14.5$  respectively. Figure 15 also shows that the  $r_e$  distributions all peak at  $r_e \sim 0.5$  kpc.

Although the average Sersic index for RR 210 field is  $n \sim 1$ , the distributions of  $M_R$  and  $r_e$  peak at fainter magnitudes ( $M_R \sim -13.5$  mag) and at smaller effective radii ( $r_e \sim 0.3$  kpc) with a noticeable lack of objects with  $r_e$  between 0.5 and 1 kpc. Furthermore the  $M_R$  distribution shows a lack of candidates in the range  $-15 \geq M_R \geq -18$  and an excess between  $-12 \geq M_R \geq -14$ . The  $\sim 2\times$  smaller distance of this pair could explain the larger number of candidates with fainter absolute magnitudes but does not account for the deficiency of objects between  $-15 \geq M_R \geq -18$ . If we further consider that the objects appear concentrated in a clump to the northwest of the pair we expect that most of them are in a separate structure and most likely a background group.

In order to further investigate the properties of candidate dwarfs we study the relations between  $M_R$ ,  $\mu_0$  and  $n$ , i.e. between distance-dependent and distance-independent quantities, shown in Figure 17. It has been suggested (Graham 2005) that these quantities should define a linear relation over a range of at least 10 magnitudes both for giant ellipticals and dwarf galaxies. We notice that the  $M_R - \mu_0$  relation for RR 210 is systematically offset by 2.3 mag from the relation in the Graham (2005) sample, although it appears to have the same slope. The magnitude shift corresponds to a shift in distance of a factor of  $\sim 3$ , suggesting that most of these objects are background galaxies which is consistent with the same inference based on their spatial distribution (see Figure 16). Notice also that the 2 confirmed members (represented as triangles in the figure) are close to the value expected from correlation.

In contrast to RR 210, several galaxies in RR 143 and RR 242 lie above the  $M_R - \mu_0$  line. Adopting the slope found by Graham (2005) and fitting the present distribution we obtain a shift in magnitude of  $\sim 1$  for both pairs probably indicating the presence of *residual* background contamination that cannot be removed without redshift measures. The RR 216 field - which shows no extended X-ray emission - is intermediate between RR 210 and RR 143/RR 242. The projected number density distribution (Figure 17) shows some

concentrations as well as an underlying smooth spatial distribution. An interpretation of the Graham (2005)  $M_R - \mu_0$  relation, which shows a shift of 1.5 mag, suggests both a larger background contamination with respect to RR 143 and RR 242 but also a larger fraction of faint galaxy companions than RR 210.

Analysis of photometric and color properties for faint galaxy populations around the pairs yields in three cases (RR 143, RR 216 and RR 242) evidence for the presence of an associated dwarf galaxy population. However, for conclusive evidence spectroscopic data are required.

## 7. Discussion

A classic problem in the study of galaxy pairs involves the difficulty to distinguish between bound and unbound systems. The problem is of great importance since a bound system implies either a long lasting co-evolution of the galaxies including: 1) matter accretion events or gas cross-fueling from gas rich spirals to ETGs (Domingue et al. 2003) or 2) their final coalescence which, according to simulations, could lead to the formation of an E-like remnant (see e.g. Barnes 1996). Significant secular evolution of the original galaxies might also occur during a chance unbound encounter although processes like cross-fuelling would be disfavored. Bars and multiple arms are typical structures developed in simulations of interacting objects and are considered indications of the secular evolution of these galaxy (see e.g. Noguchi 1987; Salo & Laurikainen 1993, and reference therein). In the case of bound systems the increased probability of merging events could link loose groups with, especially, mixed pairs containing a massive ETG. Such pairs might be “way stations” – in a hierarchical evolutionary scenario – toward the complete coalescence of a group. Several arguments indicate however that the chemical (Thomas et al. 2003), dynamical (Nipoti et al. 2003) and photometric parameters of massive ellipticals are not compatible with their formation from several major merging events distributed across a Hubble time (Meza et al. 2003).

In this context we discuss the picture suggested by photometric study of the bright members in our E+S pairs. The spiral components in RR 210 and RR 216 show unambiguous interaction signatures

(Figures 8 and 9). During encounters disc galaxies are typically more disrupted than the ellipticals because the latter are hot kinematical systems. NGC 4373 in RR 216 is a "bona fide" elliptical with an extended envelope indicated by the large effective radius (35 kpc). The long (110 kpc) and wide (56 kpc) low surface brightness plume north-east of NGC 4105 argues for an ongoing strong interaction. Simulations (see e.g. Barnes 1996) suggest that plume structures are indicative of *very recent* interaction episodes. Arguments have also been made in support of the hypothesis that the bar and tightly wound arms in IC 3290 are induced by interaction (see Reduzzi & Rampazzo 1996). Noguchi (1987) showed that bars and grand-design spiral arms induced by an interaction episode form *well after the peri-galactic passage*. We suggest that, in the light of simulations, we may interpret both features as the results of *long lasting coevolution* of the RR 216 pair members.

Neither signatures of interaction nor fine structure are found in the ETG components of RR 143 and RR 242 (NGC 2305 and NGC 5090 respectively) consistent with the same lack of evidence for perturbation in the spirals. They appear to be *relaxed systems*. ETGs in RR 210 and RR 216 display signatures of recent interaction with the presence of fine structure. Both have dust: an extended dust-lane is observed in NGC 4105. After model subtraction (see Figure 9) NGC 4373 shows the presence of ripples and plumes. We may characterize the presence of fine structure with the parameter  $\Sigma$  (see e.g. Sansom et al. 2000, and reference therein). This parameter provides an empirical measure of the optical disturbance present in a galaxy because its value is driven by a combination of effects: a) the optical strength of ripples, b) the number of detected ripples, c) the number of jets, d) an estimate of boxiness and e) the presence of X-structures. The higher the value of  $\Sigma$  the higher the morphological disturbance and the probability that the galaxy is *dynamically young*. Using the standard definition (Sansom et al. 2000), we estimate a value of  $\Sigma=0$  for NGC 2305 and NGC 5090 and conservatively  $\Sigma=1$  and  $\Sigma=3.5$  for NGC 4105 and NGC 4373 respectively. The  $\Sigma$  values of NGC 2305 and NGC 5090 are both indicative of their "relaxed" nature while that for NGC 4105, and in particular for NGC 4373, a con-

siderably less relaxed state. These values will be used below together with the X-ray information.

The X-ray picture given by *ROSAT* observations (Trinchieri & Rampazzo 2001) indicates that luminosities,  $L_X/L_B$  ratios and morphologies are very different in the 4 systems. The distribution of  $L_X$  for the four ETGs encompasses nearly the full range for early-type galaxies. The relatively faint and compact (i.e. within the optical galaxy) sources detected in RR 210 and RR 216 are consistent with emission from the evolved stellar population. RR 143 and RR 242 are more luminous and their emission is extended which is consistent with the presence of a large amount of hot gas. The XMM-Newton observations indicate that this emission encompasses both pair members (in the case of RR 143) and even another group member (NGC 5089 in RR 242). This can be interpreted as evidence that the pairs are bound and embedded in a "group-like" potential (Mulchaey 2000).

The X-ray morphologies also suggest that these two groups may be at different stages of evolution. RR 242 appears more relaxed with a more regular and azimuthally symmetric emission. The emission in RR 143, though centered on the early-type galaxy, has a clear elongation towards the companion (see Figure 3) possibly indicating dynamical effects (tidal/ram pressure stripping). A similarly shaped halo is observed in a very well studied compact group, HGC92, where both the optical and the X-ray halo convincingly suggest that accretion occurs through sequential stripping and that the smaller size companions contribute substantially to the characteristics of the diffuse halo.

Figure 18 (left panel) shows the location of our four ETG pair components in the  $\log L_B - \log L_X$  plane. We have not considered NGC 3605 (see e.g. Eracleous & Halpern 2001), NGC 3998 (see e.g. Ho et al. 1997, and reference therein) and NGC 4203 (see e.g. Ho & Ulvestad 2001, and reference therein) because their X-ray emission is dominated by LINER/AGN activity. The Sansom et al. (2000) sample includes galaxies which are dominant members of poor groups (see e.g. Helsdon et al. 2001; Mulchaey et al. 1993) and these are identified in the figure. Notice that the X-ray emission is often associated with groups containing very few galaxies, *overlapping the domain of classical pairs*. NGC 2300 in the figure is the best known example of this overlap (Mulchaey et al. 1993). This group

is dominated by a bright E+S pair (NGC 2300 and 2276) that is isolated enough to satisfy the criterion used in compilation of the Catalog of Isolated Pairs (Karachentsev 1987, KPG 127). The other members of this loose group (NGC 2268 and IC 455) are significantly fainter ( $\sim 2$  mag. Mulchaey et al. 1993).

Figure 18 (right panel) plots  $L_X/L_B$  values (O’Sullivan et al. 2001), for the same set of galaxies, as a function of the  $\Sigma$  parameter. Sansom et al. (2000) and O’Sullivan et al. (2001) discuss the anti-correlation between  $L_X/L_B$  and  $\Sigma$ . The observation that only apparently relaxed ETGs are strong X-ray emitters is argued to be (Sansom et al. 2000) consistent with the hypothesis that strong disturbances, such as mergers, cause the build up of hot gas halos over a time-scale of several gigayears. O’Sullivan et al. (2001) further suggest that some of the scatter seen in the global  $L_X$  versus  $L_B$  relation is due to the evolutionary state and past merger history of early-type galaxies.

As expected both “relaxed” galaxies (NGC 5090 and NGC 2305) as well as NGC 4373 that displays the clearest evidence of ongoing interaction are consistent with the  $L_X/L_B$ - $\Sigma$  relation derived from the Sansom et al. (2000) sample. Moderately perturbed NGC 4105 is a very weak X-ray source with a luminosity similar to NGC 474 the ETG member of Arp 227 (Rampazzo et al. 2006) which displays a complex system of shells, presumably due to strong past interactions. Read & Ponman (1998) found that relaxed remnants (about 1.5 Gyr after a merger) appear relatively devoid of hot gas after showing an increase in the emission from such gas at earlier stages (see also Hibbard et al. 1994). Fabbiano & Schweizer (1995) noted that merger remnants are X-ray weak and suggest that a merger-induced starburst could drive a galactic superwind which clears the remnant of most hot gas. After the starburst subsides the hot gas is gradually replenished by stellar mass loss (for a review, see Sarazin 1997) and, perhaps to some small extent, also by the thermalization of returning tidal debris (Hibbard & van Gorkom 1996).

The above considerations suggest that RR 143 and RR 242 form bound structures on the basis of their extended X-ray emission. Note however that, at odds with RR 242, RR 143 is a very poor struc-

ture without luminous companions. RR 210 and RR 216 do not have extended X-ray emission but both have some luminous companions (see Figures 8 and Figure 9) and probably represent the *active* part of very poor and loose *evolving* groups. The *activity* is seen in the optically distorted morphology traced by low luminosity plumes. The presence of these structures, at least in RR 216, could be interpreted in terms of a long lasting co-evolution of the pair.

Additional arguments in favour of the bound nature of some groups have been provided by Zabludoff & Mulchaey (1998). They found a significantly higher number of faint galaxies ( $\approx 50$  members down to magnitudes as faint as  $M_B \approx -14 + 5\log_{10} h_{100}$ ) in groups with a hot IGM. This finding led to the idea of defining aggregates in LDE according to their X-ray properties, ETG fraction and faint galaxy population. In order to clarify the proposed connection between poor groups and isolated ellipticals we used our wide field images to identify candidate dwarf galaxy populations around our pairs. We identify a relatively high number of potential members in three out of four pairs (e.g. in RR 143, RR 216 and RR 242) while the faint galaxy sample detected in the RR 210 field does not appear to be associated with the pair.

Both the X-ray luminosities of RR 242 and RR 143, and the presence of a large *candidate* faint companion populations argue in favor of the hypothesis that these are bound systems. In the Zabludoff (1999) scheme they can be considered as *evolved systems* with X-ray emission centered on the bright E. RR 216 is probably an intermediate example of an *evolving* groups since its elliptical is quite perturbed with a modest hot IGM component and possibly large number of faint companions. The X-ray luminosity in RR 210 does not support any hot IGM component as in the case of Arp 227 (Rampazzo et al. 2006). The suggested lack of a faint galaxy population suggests that it is either unbound or in a very early-phase of its evolution.

We would like to add some considerations on the evolution of the ETGs in these systems. From the optical point of view, all the ellipticals in our sample are evolved, luminous and massive <sup>5</sup>, with

<sup>5</sup>The velocity dispersion,  $\sigma$ , does not have a one-to-one rela-

an average  $\langle \sigma \rangle = 254 \pm 34 \text{ km s}^{-1}$  (i.e. corresponding to  $M = 3.47 \times 10^{11} M_{\odot}$ ).

Our systems have masses and environmental properties similar to the class of “fossil groups” that is now emerging in the literature, *e.g.* NGC 1132 (Tonry & Davies 1981), NGC 6482 (Faber et al. 1989) or ESO 3060170 (Beuing et al. 2002). This is of special importance given the recent evidence of (Clemens et al. 2006) which finds that the timing of the formation of early-type galaxies is determined by the environment but the details of the process of star formation are entirely regulated by the galaxy mass. Since these two quantities – environmental density and galaxy masses – are very similar throughout our sample we suggest that the difference in their X-ray emission could be explained in terms of the present evolutionary phase of the system (see *e.g.* Sansom et al. 2000; O’Sullivan et al. 2001).

## 8. Summary and conclusions

We present an optical and X-ray study of four E+S pairs, RR 143, RR 210, RR 216 and RR 242 and their environments with the main aim to assess their evolutionary histories. We have obtained new XMM-Newton data for 2 pairs, RR 143 and RR 242, that complement the ROSAT data already presented the other two Trinchieri & Rampazzo (2001). With these data:

- We confirm the presence of extended X-ray emission in both RR 143 and RR 242 with luminosities  $L_X \sim 3 \times 10^{41} [\text{erg s}^{-1}]$ .
- The emission in RR 143 is centered on the ETG but is asymmetric and elongated towards the late type companion with a total extension to  $r \sim 500''$  (120 kpc).
- The large scale emission from RR 242 is more regular and extends out to  $700''$  (160 kpc). A low

---

tionship with the mass of the galaxy. Recent work by Cappellari et al. (2006) has investigated the relation between the galaxy mass-to-light (M/L) ratio and the line-of-sight component of the velocity dispersion with the effective radius. They provide relations (their equations 7 and 10) which allow a transformation from measured velocity dispersion to galaxy mass;

$$M_{10} = (16.5 \pm 7.8) \sigma_{200}^{3.11 \pm 0.43} \quad (3)$$

where  $M_{10}$  is the galaxy mass in units of  $10^{10} M_{\odot}$  and  $\sigma_{200}$  is the velocity dispersion in units of  $200 \text{ km s}^{-1}$ . The errors have been propagated from the parameter values found by Cappellari et al. (2006).

luminosity ( $L_X \sim 10^{41} \text{ erg s}^{-1}$ , 2.0-10 keV), mildly absorbed ( $N_H \sim 10^{22} \text{ cm}^{-2}$ ) AGN is present at the center of RR 242, together with a moderately sub-solar,  $\sim 0.6 \text{ keV}$ , plasma emission, possibly due to the central galaxy.

We considered the X-ray properties together with the results of a V, R photometric study of the brighter members and a search for *candidate* faint companions.

- We find that the ETGs in X-ray luminous pairs appear to be relaxed objects while the X-ray faint ETGs display unambiguous signatures of ongoing interaction.
- We identified a sample of faint galaxies among which we may find objects possibly associated with our pairs. We considered the likelihood of physical association with the pairs and find that a small fraction of the detected objects are likely faint companions except in the case of RR 210 where even a larger background contamination is suspected.

In the light of current ideas we suggest that:

- Both X-ray luminous E+S pairs RR 143 and RR 242 are likely the dominant members of *evolved* poor groups. Only a few luminous members are associated with these systems although our study suggests that they might have a significant population of faint member.
- RR 210 and RR 216 are likely the dominant members of *evolving* groups.
- At odds with their optical, kinematic (mass) and environmental similarities, the ETGs in our E+S pairs have remarkably different X-ray properties. We suggest that this can be explained either in terms of the present evolutionary phase of the system or the past histories of the ETGs.

Spectroscopic observations currently on-going with ESO VLT + VIMOS will provide redshifts for the faint galaxy populations that will identify associated dwarf populations and allow us to better study the evolutionary stage of these systems.

RG and RR thank the INAF-Osservatorio Astronomico di Padova and the Institut für Astronomie Universität Wien, respectively, for the kind hospitality during the paper preparation. RG, RR and WWZ acknowledge the support of the Austrian and Italian Foreign Offices in the framework science and technology bilateral collaboration (project number 25/2004). RG and WWZ

acknowledge the support of the Austrian Science Fund (project P14783). RR and GT acknowledge the partial support of the Agenzia Spaziale Italiana under contract ASI-INAF I/023/05/0. This research has made use of the NASA/IPAC Extragalactic Database (NED) which is operated by the Jet Propulsion Laboratory, California Institute of Technology, under contract with the National Aeronautics and Space Administration. The Digitized Sky Survey (DSS) was produced at the Space Telescope Science Institute under U.S. Government grant NAG W-2166. The images of these surveys are based on photographic data obtained using the Oschin Schmidt Telescope on Palomar Mountain and the UK Schmidt Telescope. The plates were processed into the present compressed digital form with the permission of these institutions. This research has made use of SAOImage DS9, developed by Smithsonian Astrophysical Observatory.

Facilities: XMM-Newton, 2.2 ESO + WFI.



### A. X-ray Individual sources

We used standard detection procedure to derive parameters for other X-ray sources detected in the fields of RR 143 and RR 242. We considered the 0.5-2.0; 2.0-10.0; and 0.5-10.0 keV bands and all three detectors. Since the detection of serendipitous sources in the fields was not a motivation for this work we limit ourselves to sources above a maximum likelihood threshold of 15 in order to minimize contamination from spurious sources. For this reason we did not consider sources within  $200''$  of the center of the emission (except for #17, #18, and #20 in RR 143 clearly visible on the images) where the algorithm finds a large number of sources likely to be fluctuations within the extended emission. Fluxes are determined assuming a power law spectrum with  $\Gamma=1.7$  and are corrected for line-of-sight absorption. When possible we use the PN data to determine count rates and fluxes, however when the sources fall on a CCD gap or defect we use the MOS1 data (see last column in the tables). Detected sources are listed in Tables 9 and 10.

Several of the X-ray sources coincide with faint optical counterparts. However, comparison between the candidate member lists with the X-ray source lists indicate coincidence only between galaxy # 13627 in RR 242, and source #23. This is not surprising, since the galaxies are all significantly fainter than the pair members and are not expected to be detectable, unless they contain an active nucleus. Most other X-ray sources are likely to be background AGNs.

## REFERENCES

- Annibali, F., Bressan, A., Rampazzo, R., Danese, L. & Zeilinger, W. W. 2006, A&A, submitted.
- Arp, H. C. & Madore, B.F. 1987, Catalogue of Southern Peculiar Galaxies and Associations, V. 1-2, Cambridge University Press
- Barnes, J. 1996, Galaxies: Interactions and Induced Star Formation (26th Saas-Fee Advanced Course) (New York: Springer), 275
- Belsole, E., Sauvageot, J.-L., Ponman, T. J. & Bourdin, H. 2003, AA, 398, 1
- Bertin, E. & Arnouts, S. 1996, AAS, 117, 393
- Bettoni, D., Falomo, R., Fasano, G. & Govoni, F. 2003, AA, 399, 869
- Beuing, J., Bender, R., Mendes de Oliveira, C., Thomas, D. & Maraston, C. 2002 A&A, 395, 431
- Binggeli, B., Sandage, A. & Tarenghi, M. 1984, AJ, 89, 64
- Caon, N., Macchetto, D. & Pastoriza, M. 2000, ApJS, 127, 39
- Cappellari, M., Bacon, R., Bureau M., Damen, M. C., Davies, R. L., de Zeeuw, P. T., Emsellem, E., Falcon-Barroso, J., Krajnovic, D., Kuntschner, H., McDermid, R. M., Peletier, R. F., Sarzi M., van den Bosch, R. C. E. & van de Ven, G. 2006, MNRAS, 366, 1151
- Carollo, M., Danziger, I. J. & Buson, L. M. 1993, MNRAS, 265, 553
- Chapman, S.C., Smail, I., Blain, A. W. & Ivison, R. J. 2004, ApJ, 614, 671
- Ciotti, L., Pellegrini, S., Renzini, A. & D'Ercole, A. 1991, ApJ, 376, 380
- Clemens, M. S., Bressan, A., Nikolic, B., Alexander, A., Annibali, F. & Rampazzo, R. 2006, MNRAS, submitted
- Colbert, J. W., Mulchaey, J. S. & Zabludoff, A. I. 2001, AJ, 121, 808
- De Lucia G., Springel, V., White, S. D. M., Croton, D. & Kauffmann, G. 2006, MNRAS, 366, 499
- De Souza, R.E., Gadotti, D.A. & Dos Anjos S. 2004, ApJS, 153, 411
- Dickens, R. J., Currie, M. J. & Lucey, J. R. 1986, MNRAS, 220, 679
- Domingue, D. L., Sulentic, J. W. & Durbala, A. 2005, AJ, 129, 2579
- Domingue, D. L., Sulentic, J. W., Xu, C., Mazarrella, J., Gao Y. & Rampazzo, R. 2003, AJ, 125, 555
- Dressler, A. 1980, ApJ, 236, 351
- Dressler, A. 1984, ApJ, 281, 512
- Ellis, S.C. & Bland-Hawthorn, J. 2006, astro-ph/06025573
- Eracleous, M. & Halpern, J. P. 2001, ApJ, 554, 240
- Fabbiano, G., & Schweizer, F. 1995, ApJ, 447, 572
- Faber, S. M. 1973, ApJ, 179, 731
- Faber, S. M., Wegner, G. Burstein, D., Davies, R. L., Dressler, A., Lynden-Bell, D. & Terlevich, R. J. 1989, ApJS, 69, 763
- Falcon-Barroso, J. et al. 2005, NewAr, 49, 515
- Franx, M. et al. 2003, ApJ, 587, L79
- Gonzales, A.H., Zabludoff, A. I. & Zaritsky, D. 2005, ApJ, 618, 195
- Govoni, F., Falomo, R., Fasano, G. & Scarpa, R. 2000, AAS, 143, 369
- Graham, A. W. 2005, in Near-fields cosmology with dwarf elliptical galaxies, IAU Colloquium No. 198, H. Jerjen and B. Binggeli eds., Cambridge University Press 2005, pp.303-310
- Grützbauch, R., Kelm, B., Focardi, P., Trinchieri, G., Rampazzo, R. & Zeilinger, W. W. 2005, AJ, 129, 1832.
- Grützbauch, R., Annibali, F., Bressan, A., Focardi, P., Kelm, B., Rampazzo, R. & Zeilinger, W. W. 2005, MNRAS, 364, 146.
- Hamabe, M. & Kormendy, J. 1987, IAUS, 127, 379
- Helsdon, S.F., Ponman, T.J., O'Sullivan, E. & Forbes, D.A. 2001, MNRAS, 325, 693

- Henriksen, M. & Cousineau, S. 1999, *ApJ*, 511, 595
- Hernandez–Toledo, H. M., Dultzin-Hacyan, D. & Sulentic, J. W. 2001, *AJ*, 121, 1319
- Hibbard, J. E., Guhathakurta, P., van Gorkom, J. H. & Schweizer, F. 1994, *AJ*, 107, 67
- Hibbard, J. E. & van Gorkom, J. 1996, *AJ*, 111, 655
- Ho, L.C., Filippenko, A. V., Sargent W.L.W. & Peng, C.Y. 1997, *ApJS*, 112, 391
- Ho, L.C. & Ulvestad, J.S. 2001, *ApJS*, 133, 77
- Jedrzejewski, R. 1987, *MNRAS*, 226, 747
- Jones et al. 2003, *MNRAS*, 343, 627
- Karachentsev, I.D. 1987, *Dvoinye Galaktiki*, (Nauka Moskow)
- Khosroshahi, H. G. Raychaudhury, S., Ponman, T. J., Miles, T. A. & Forbes, D. A., 2004, *MNRAS*, 349, 527
- Landolt, A. U. 1992, *AJ*, 104, 340
- Lloyd, B.D., Jones, P.A. & Haynes, R.F. 1996, *MNRAS*, 279, 1187
- Longhetti, M., Rampazzo, R., Bressan, A. & Chiosi C. 1998, *AAS*, 130, 251
- Longhetti, M., Rampazzo, R., Bressan, A. & Chiosi C. 1998, *AAS*, 130, 267
- Longhetti, M., Bressan, A., Chiosi, C. & Rampazzo, R. 1999, *AA*, 345, 419
- Llyod, B.D., Jones, P.A. & Haynes, R.F. 1996, *MNRAS*, 279, 1187
- Meza, A., Navarro, J. F., Steinmetz, M. & Eke, V. R., 2003, *ApJ*, 590, 619
- Miller, N. A., Ledlow, M. J., Owen, F. N. & Hill, J. M. 2002 *AJ*, 123, 3018
- Mulchaey, J. S., Davis, D. S., Mushotzky, R.F. & Burstein, D. 1993, *ApJ*, 404, L9
- Mulchaey, J. S., Davis, D.S., Mushotzky, R.F. & Burstein, D. 1996, *ApJ*, 456, 80
- Mulchaey, J. S. & Zabludoff, A.I. 1999, *ApJ*, 514, 133
- Mulchaey, J. S. 2000, *ARAA*, 38, 289
- Mulchaey, J. S., Davis, D. S., Mushotzky, R. F. & Burstein, D., 2003, *ApJS*, 145, 39
- Nevalainen, J., Markevitch, M. & Lumb, D. 2005, *ApJ*, 629, 172
- Nipoti, C., Londrillo, P. & Ciotti, L. 2003, *MNRAS*, 342, 501
- Noguchi, M. 1987, *MNRAS*, 228, 635
- Noguchi, M. 1988, *AA*, 203, 259
- Nolan, L. A., Ponman, T. J., Read, A. M. & Schweizer, F. 2004, *MNRAS*, 353, 221.
- O’Sullivan, E., Forbes, D.A. & Ponman, T. J. 2001, *MNRAS*, 328, 461
- Ota, N., Morita, U., Kitayama, T. & Ohashi, T. 2004, *PASJ*, 56, 753
- Peng, C. Y., Ho, L. C., Impey, C. D. & Rix, H. 2002, *AJ*, 124, 266
- Rampazzo, R. 1988, *AA*, 204, 81
- Rampazzo, R. & Sulentic, J. W. 1992, *AA*, 259, 43
- Rampazzo, R., Covino, S., Trinchieri, G. & Reduzzi, L. 1998, *AA*, 330, 423
- Rampazzo, R., Alexander, P., Carignan, C. et al. 2006, *MNRAS*, in press
- Read, A.M. & Ponman, T.J. 1998, *MNRAS*, 297, 143
- Read, A.M. & Ponman, T.J. 2003, *AA*, 409, 395
- Reduzzi, L. & Rampazzo, R. 1995, *ApLC*, 30, 1
- Reduzzi, L. & Rampazzo, R. 1996, *AAS*, 116, 515
- Reduzzi, L., Longhetti, M. & Rampazzo, R. 1996, *MNRAS*, 282, 149
- Rizzi, L. 2003, Research Doctorate Thesis, University of Padua
- Rose, J.A. 1984, *AJ*, 89, 1238

- Rose, J.A. 1985, AJ, 90, 1927
- Sadler, E. M. & Sharp, N. A. 1984, AA, 133, 216
- Salo, H. 1991, AA, 243, 118
- Salo, H. & Laurikainen, E. 1993, ApJ, 410, 586.
- Samurović, S. & Danziger, I. J. 2005, MNRAS, 363, 769
- Sansom, A. E., Hibbard, J. E. & Schweizer, F. 2000, AJ, 120, 1946
- Sarazin, C. L. 1997, The Nature of Elliptical Galaxies, ASP Conf. Ser. 116, M. Arnaboldi, G. S. Da Costa & P. Saha Eds., San Francisco: ASP, 375
- Sersic, J. L. 1968, Atlas de Galaxias Australes, Observatorio Astronomico, Cordoba
- Sulentic, J. W. et al. 2006, AA, 449, 937
- Thomas, D., Maraston, C. & Bender, R., 2003, Astrophys. & Space Science, 281, 371
- Thomas, D., Maraston, C., Bender, R. & de Oliveira, C. M. 2005, ApJ, 621, 674
- Tonry, J. & Davies, M. 1981, ApJ, 246, 666
- Treu, T. et al. 2005, ApJ, 622, L5
- Trinchieri, G. & Rampazzo, R. 2001, AA, 374, 454
- Trinchieri, G., Sulentic, J., Breitschwerdt, D. & Pietsch, W. 2003, AA, 401, 173
- Tully, B.R. 1988, Nearby Galaxy Catalogue, Cambridge University Press
- Valdes, F. G. 1998, Astronomical Data Analysis Software and Systems VII, ASP Conf. Ser. 145, R. Albrecht, R. N. Hook, & H. A. Bushouse Eds., San Francisco: ASP, 7
- Verdes-Montenegro, L., Sulentic, J., Lisenfeld, U., Leon, S., Espada, D., Garcia, E., Sabater, J. & Verley, S. 2005, AA, 436, 443
- Vikhlinin et al. 1999, ApJ, 520, 1
- Visvanathan, N. & Sandage, A. 1977, ApJ, 216, 214
- Wilms, J., Allen, A. & McCray, R. 2000, ApJ, 542, 914
- Zabludoff, A. & Mulchaey, J. 1998, ApJ, 496, 39
- Zabludoff, A. 1999, IAU Symp. 192, eds. P. White-lock and R. Cannon, 433
- Zacharias, N., et al. 2000, AJ, 120, 2131

---

This 2-column preprint was prepared with the AAS L<sup>A</sup>T<sub>E</sub>X macros v5.2.

Fig. 1.— Iso-intensity contours of the adaptively smoothed X-ray emission from RR 143 (NGC 2305/NGC 2307; left) and RR 242 (NGC 5090/NGC 5091; right) detected with XMM-Newton. Contours are superposed on R-band images obtained with the 2.2m MPG-ESO telescope (see text). The galaxy west of NGC 5090 is NGC 5082.

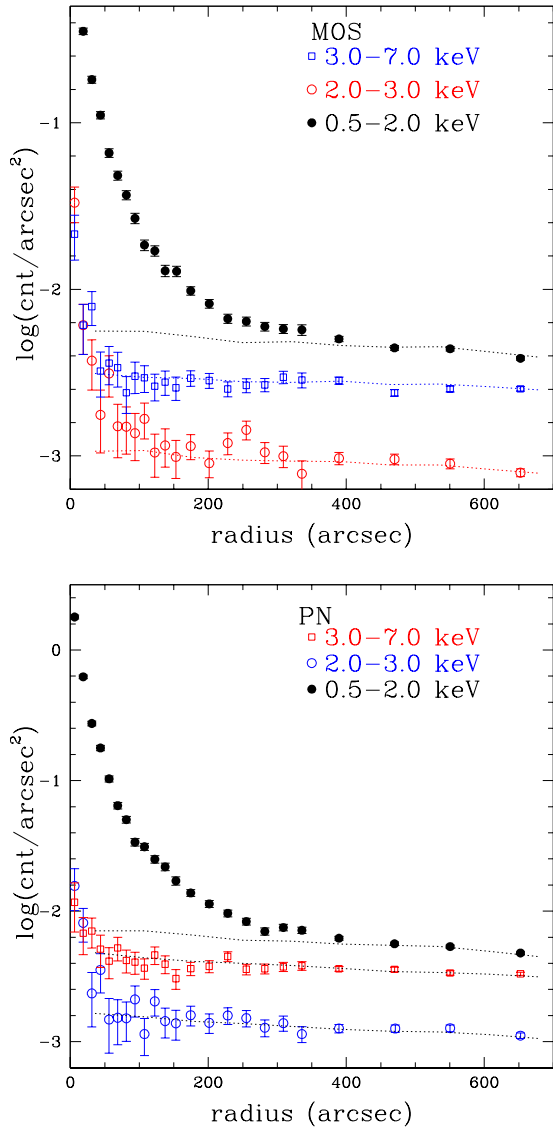


Fig. 2.— Surface brightness profile of the raw XMM data in different energy bands, centered on NGC 2305, the early-type member of the pair RR 143. MOS and PN are shown separately. The background shapes relative to each profile are also plotted.

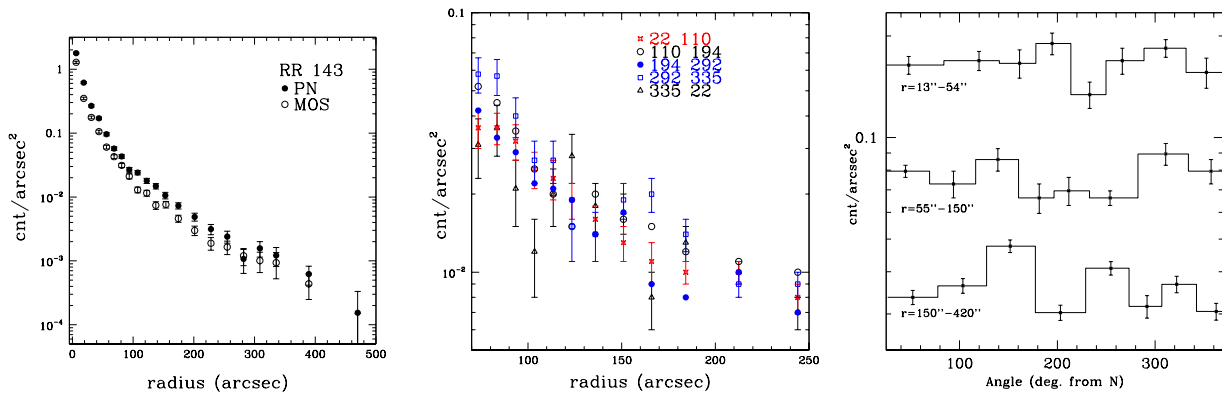


Fig. 3.— Surface brightness profile of the net emission in RR 143: azimuthally averaged from MOS and PN separately (left), in different quadrants (middle) and at different angles and radial distance from the center (right). All plots are in the 0.5-2.0 keV band.

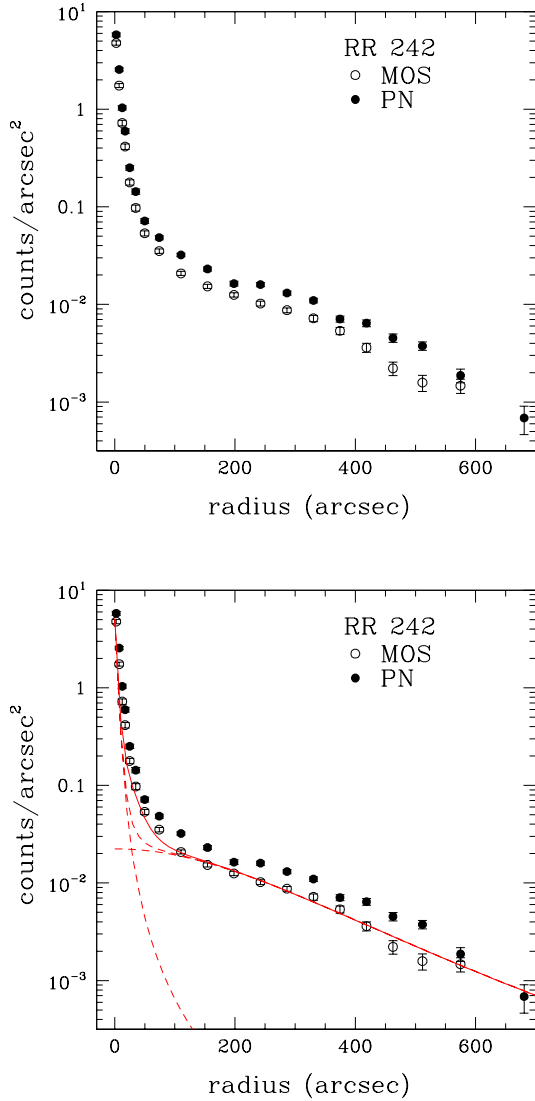


Fig. 4.— Surface brightness profile of the azimuthally averaged net emission in RR 242, in the 0.5-2.0 keV band, from MOS and PN separately (left). A three component model, due to the sum of the MOS point spread function (PSF) and two  $\beta$ -profile functions with  $r_c = 420''$  and  $r_c = 45''$  and  $\beta \sim 1$ , is shown as a solid line. The PSF and the larger  $\beta$ -profile are also plotted as a dashed line (right panel).

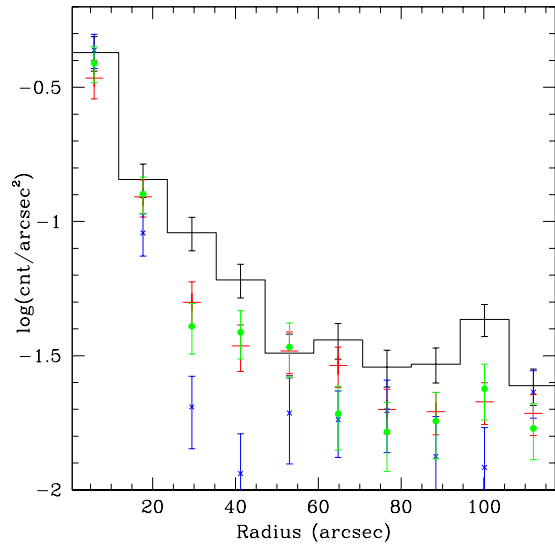


Fig. 5.— Radial profile of the emission centered on NGC 5082 in 4 different azimuthal sectors. The data are in the 0.5-2 keV energy range. The histogram refers to the 27-117° quadrant, red crosses to 177-207°, blue crosses to 207-297° and green dots to 297-27° (clockwise from N).



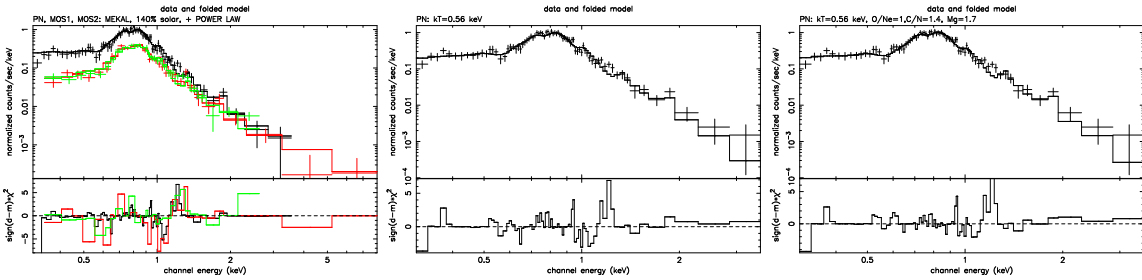


Fig. 6.— Spectral distribution of the diffuse emission in RR 143. Note that since the emission extends over several CCDs in EPIC-PN, spectral data are obtained from smaller regions that would fit within a single CCD. To compensate for different areas in EPIC-PN and EPIC-MOS, the relative normalization is left free. Top: EPIC-PN and EPIC-MOS data. The model is a MEKAL ( $kT=0.5$  keV, 100 % solar abundances) plus and power law (fixed  $\Gamma = 1.5$ ), with galactic  $N_H$ . Middle and bottom: PN data only. The model is a  $kT=0.5$  keV MEKAL, 90% abundances with ratios between elements fixed at the solar values, and a  $kT=0.5$  keV VMEKAL, with Mg at 170%, O–Ne at 100% and C–N at 140% of the solar value, respectively.

Fig. 7.— (*large right panel*) WFI R-band image of RR 143 and its environment. (*top left panel*) Finding chart of spectroscopically confirmed members of the RR 143 system within the FoV. Galaxies are marked with symbols sized according to their absolute magnitude. Labels 1 and 2 stand for NGC 2305 and for NGC 2307 respectively. (*mid left panel*) Residual image of the central pair after the subtraction of a model of the dominant ETG member; (*bottom left panel:*) Residual image after the subtraction of the gaussian smoothed image.

Fig. 8.— (*large right panel*) WFI R-band image of RR 210 and its environment. (*top left panel*) Finding chart of spectroscopically confirmed members of the RR 210 system within the FoV. Galaxies are marked with symbols sized according to their absolute magnitude. NGC 4105 (label 1), NGC 4106 (label 2), 2MASX J12065029-2936236 (label 3:  $V_{hel} = 2019$  km/s), 2MASX J12063106-2951336 (label 4:  $V_{hel} = 2132$  km/s), IC 2996 (label 5:  $V_{hel} = 2256$  km/s). (*mid left panel*) Residual image of the central pair after the subtraction of a model of the dominant ETG member; (*bottom left panel:*) Residual image after the subtraction of the gaussian smoothed image.

Fig. 9.— (*large right panel*) WFI R-band image of RR 216 and its environment. (*top left panel*) Finding chart of spectroscopically confirmed members of the RR 216 system within the FoV. Galaxies are marked with symbols sized according to their absolute magnitude. NGC 4373 (label 1), IC 3290 (label 2), 6dF J1225118-393507 (label 3:  $V_{hel} = 2140$  km/s), ESO 322-IG 002 (label 4:  $V_{hel} = 3264$  km/s). (*mid left panel*) Residual image of the central pair after the subtraction of a model of the dominant ETG member; (*bottom left panel:*) Residual image after the subtraction of a model of the dominante ETG member; (*bottom left panel:*) Residual image after the subtraction of the gaussian smoothed image.

Fig. 10.— (*large right panel*) WFI R-band image of RR 242 and its environment. (*top left panel*) Finding chart of spectroscopically confirmed members of the RR 242 system within the FOV. Galaxies are marked with symbols sized according to their absolute magnitude. NGC 5090 (label 1), NGC 5091 (label 2), NGC 5082 (label 3:  $V_{hel} = 3896$  km/s), NGC 5090B (label 4:  $V_{hel} = 4248$  km/s), ESO 270- G 001 (label 5:  $V_{hel} = 2960$  km/s), 2MASX J13201668-4327195 (label 6:  $V_{hel} = 3088$  km/s). (*mid left panel*) Residual image of the central pair after the subtraction of a model of the dominant ETG member; (*bottom left panel:*) Residual image after the subtraction of the gaussian smoothed image.

Fig. 11.— Surface photometry of the elliptical pair member: *from top to bottom* surface brightness, ellipticity, position angle, fourier coefficients and color profile.

Fig. 12.— Detection of diffuse light in RR 216. An extended plume indicative of on-going strong interaction is visible in the NE quadrant, with the tip of the plume wrapping towards S.

Fig. 13.—  $(V-R)$  color-magnitude relation for all pairs/groups. The bold line is the color magnitude relation for the Virgo cluster (shifted to the pairs redshift), while the dashed line represents the color restriction at  $(V-R) = 1$  applied to exclude background objects. The spectroscopic confirmed pair/group member galaxies are labeled as in Figures 7 - 10.

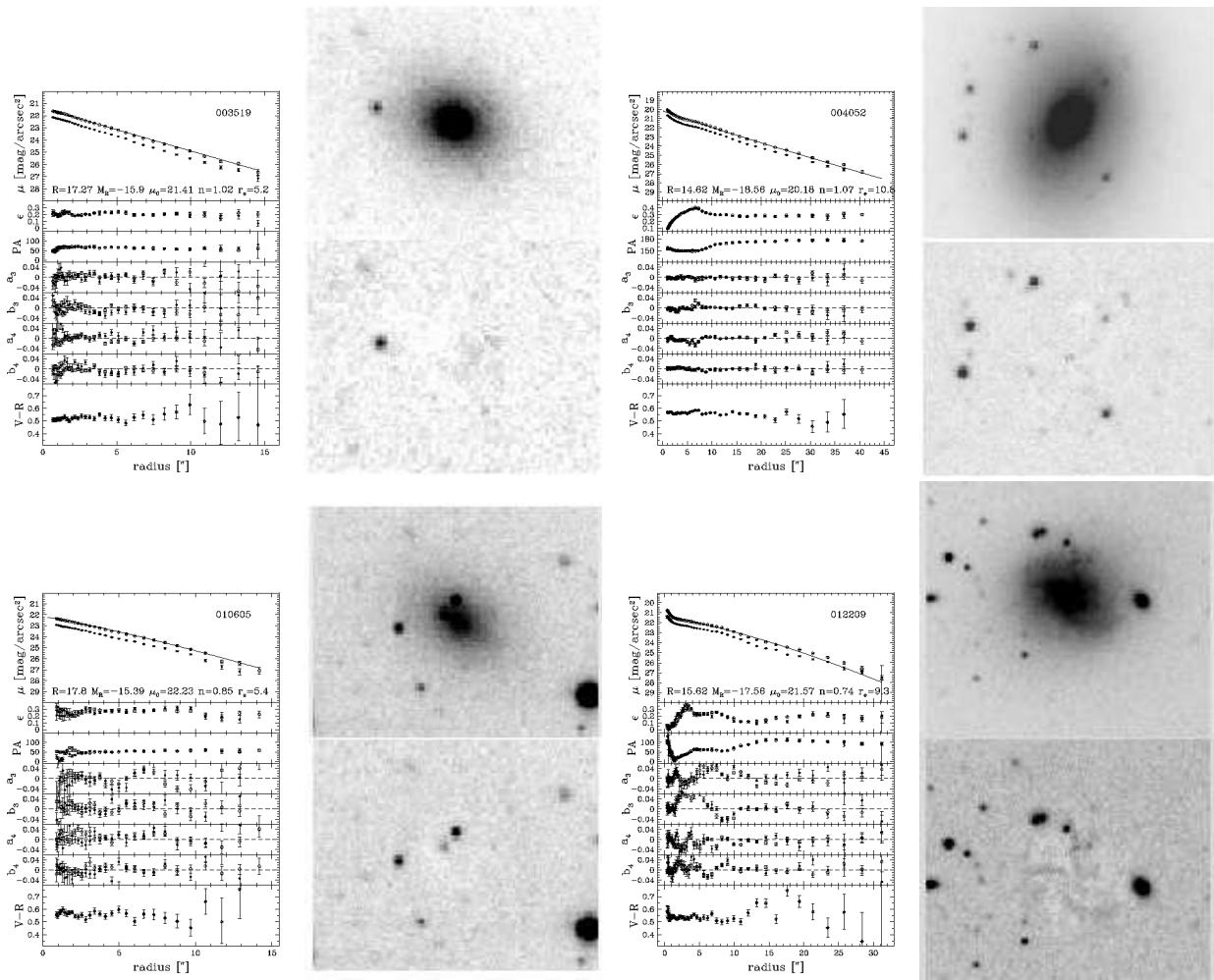


Fig. 14.— A sample of candidate members. Luminosity profiles obtained with the IRAF-ELLIPSE procedure (left panels), R band image and residual image after automated model subtraction with the GALFIT package (top and bottom right panels). The model parameters for each object are provided in the surface brightness panels. The solid line represents the surface brightness profile of the GALFIT-model.

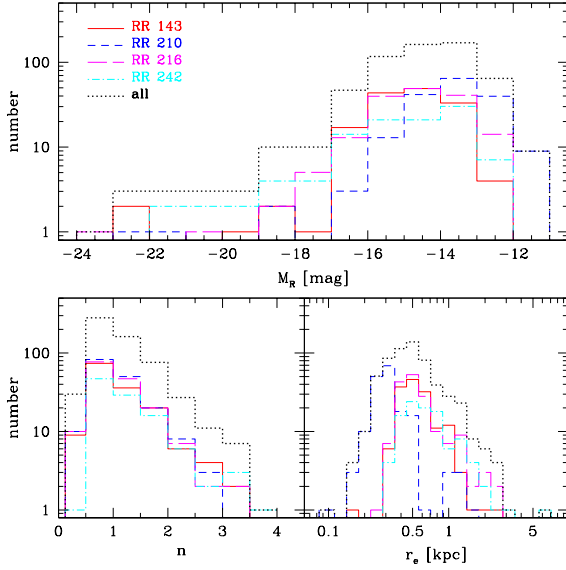


Fig. 15.— Distribution of absolute R band magnitudes (*top*), effective radii (*bottom right*) and Seric indices  $n$  (*bottom left*) of the pair/group members and possibly associated faint galaxy population.

Fig. 16.— Surface density maps of the candidate faint members selected according to the color magnitude relation shown in Figure 13: **RR 143** (*top left*), **RR 210** (*top right*), **RR 216** (*bottom left*), **RR 242** (*bottom right*). The positions of (bright) confirmed members of each galaxy system are indicated with a symbol size according to their absolute magnitude (Figures 7 - 10 provide the identifications).

Fig. 17.— Relations between central surface brightness  $\mu_0$ , Seric index  $n$  and absolute R band magnitude. The bold lines define the relations for a large sample of early type galaxies taken from Graham (2005). Large symbols represent spectroscopic confirmed member galaxies (see Figures 7 - 10 for identifications).

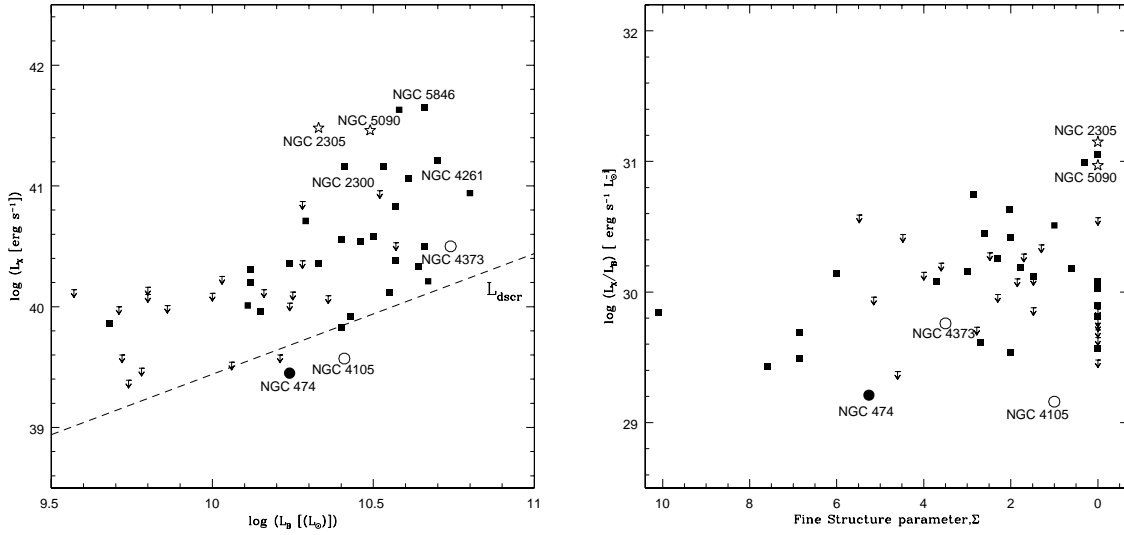


Fig. 18.— (left panel) Location of the early-type galaxies members of our systems in the  $L_B - L_X$  plane. With open stars we plot the location of our ETGs observed with XMM-Newton, with open circles we plot NGC 2305 and NGC 4373 observed with ROSAT by Trinchieri & Rampazzo (2001). For comparison we plot also early-type galaxies with fine structure, indicative of *dynamically young* galaxies, from the sample of Sansom et al. (2000). Notice in particular the location of NGC 474 (Rampazzo et al. 2006) which has a large system of shells and is interacting with the spiral NGC 470. X-ray luminosities are taken from the O’Sullivan et al. (2001) compilation. We have also used their recipe to re-calculate the luminosity, given in Table 3. We have labeled some galaxies in this sample that are members of poor groups (see e.g. Helsdon et al. 2001). The dashed line ( $L_{dscr}$ ) represents the expected contribution from discrete stellar X-ray sources from Ciotti et al. (1991). Filled squares are detections and arrows denote upper limits. (right panel) Position of galaxies in the plot of normalized X-ray luminosity versus fine structure parameter  $\Sigma$  for early type galaxies.

TABLE 1  
OVERVIEW OF THE PAIRS AND THEIR MEMBERS

	RR 143		RR 210		RR 216		RR 242		
	NGC 2305	NGC 2307	NGC 4105	NGC 4106	IC 3290	NGC 4373	NGC 5090	NGC 5091	notes
ESO ident	870440	870450	4400540	4400560	3220040	3220060	2700020	2700040	
RA (2000)	06 48 36	06 48 50	12 06 41	12 06 45	12 25 09	12 25 18	13 21 12	13 21 18	
Decl. (2000)	-64 16 24	-64 20 01	-29 45 42	-29 46 06	-39 46 31	-39 45 37	-43 42 16	-43 43 10	
Morphol. Type	E2: pec	SB(rs)ab	E3	SB(s)0+	SB(s)a	SAB(rs)0-:	E2	Sb pec sp	[1]
<b>App. magnitude and color:</b>	NGC 2305	NGC 2307	NGC 4105	NGC 4106	IC 3290	NGC 4373	NGC 5090	NGC 5091	notes
$B_T$	12.74	12.92	11.60	12.36	12.96	11.90	12.57	13.91	[1]
$(B-V)_T^0$	0.92	0.77	0.87	0.90		0.86			[1]
$(J-H)_{2MASS}$	0.68	0.68	0.53		0.63	0.66	0.79		[1]
$(H-K)_{2MASS}$	0.22	0.30	0.32		0.36	0.27	0.23		[1]
IRASS $_{12\mu}$ [Jy]	<0.029	<0.089	<0.023	<0.023		<0.027	0.120±0.031		[1]
IRAS $_{25\mu}$ [Jy]	<0.024	<0.081	<0.039	<0.029		<0.030	0.200±0.028		[1]
IRAS $_{60\mu}$ [Jy]	<0.039	0.271	0.260±0.039	0.220±0.022		<0.044	0.170±0.045		[1]
IRAS $_{100\mu}$ [Jy]	<0.103	1.572	0.830±0.152	0.710±0.170		<0.191	0.860±0.477		[1]
<b>X-ray and B luminosity:</b>	NGC 2305	NGC 2307	NGC 4105	NGC 4106	IC 3290	NGC 4373	NGC 5090	NGC 5091	notes
$\log L_X$ (0.5-2.0 keV) [erg s $^{-1}$ ]	41.6		39.6	39.1		40.5		41.0	[8]
$\log L_B$ [ $L_\odot$ ] [erg s $^{-1}$ ]	10.4		10.4	10.1		10.7		10.5	[8]
$\log L_X/L_B$ [erg s $^{-1}$ $L_\odot^{-1}$ ]	31.2		29.2	29.0		29.8		30.6	[8]
<b>Galaxy structure:</b>	NGC 2305	NGC 2307	NGC 4105	NGC 4106	IC 3290	NGC 4373	NGC 5090	NGC 5091	notes
Mean Eff. Surf. Bright. $\mu_e$ (B)	20.83±0.44	22.44 ±0.30	21.27±0.36	21.48±0.94	22.26±0.35	21.26±0.64	21.58±0.56	21.86±0.35	[2]
Average ellipticity $\langle \varepsilon \rangle$	0.29	0.07	0.25[4]	0.33	0.21	0.3[4]	0.15	0.60	[2]
$\langle P.A. \rangle$ ( $\Delta P.A.$ ) [deg]	142 ( $\approx 40$ )[4]		143 ( $< 10$ )[4]	94.2 ( $\approx 50$ )[4]	22.5	38 ( $< 10$ )[4]	109	122	
shape parameter [a4/a]	irr		irr	irr		disky			[4]
<b>Kinematical parameters:</b>	NGC 2305	NGC 2307	NGC 4105	NGC 4106	IC 3290	NGC 4373	NGC 5090	NGC 5091	notes
Hel. Sys. Vel. [km s $^{-1}$ ]	3241±20 [5]	3515±27	1912±23 [7]	2170±18 [7]	3342	3396	3421	3529	[1]
Vel.disp. $\sigma_0$ [km s $^{-1}$ ] stars	244		277±22[7]	253±17[7]		234±23	272±27		[3]
<b>Pairs parameters:</b>	RR 143		RR 210		RR 216		RR 242		
Arp-Madore ident.	AM0648-641		AM1204-292		AM1222-392				
Projected separation ['] (kpc)	234 (51.1)		59 (7.7)		118 (25.7)		77 (17.2)		[6]
$\Delta V$ [km s $^{-1}$ ]	274		258		54		108		
Adopted distance [Mpc]	45		27		45		46		

NOTE.—In general the photometric, kinematical and structural data are derived from NED [1], LEDA [2] and Hypercat <http://www-obs.univ-lyon1.fr/hypercat> [3] compilations. Detailed studies of some objects have been done by our group and labeled as follows: Reduzzi & Rampazzo (1996) [4], Rampazzo (1988) [5], Reduzzi & Rampazzo (1995) [6], Longhetti et al. (1998b) [7], the original ROSAT data published in Trinchieri & Rampazzo (2001) are converted to the 0.5 - 2 keV band and to  $H_0=75 \text{ km s}^{-1} \text{ Mpc}^{-1}$  [8]. The shape parameter  $a_4/a$  is indicated as boxy ( $a_4/a < 0$ ), disky ( $a_4/a > 0$ ) and irregular (irr) when there is no definite trend in the shape profile with radius. The adopted distance is obtained using  $H_0=75 \text{ km s}^{-1} \text{ Mpc}^{-1}$ .

TABLE 2  
LOG-BOOK OF XMM-NEWTON OBSERVATIONS.

Pair	Obs. date	Original Time PN/MOS	Used livetime [s]
RR 143	2003-10-19	9325/11850	7289/9250
RR 242	2003-07-17	18032/21650	11794/14318

TABLE 3  
BASIC X-RAY PROPERTIES OF THE EXTENDED COMPONENT

Object	extension		counts	count	flux	log $L_X$	Spectral parameters †
	[']	[kpc]	[0.5-2.0keV]	rate	[0.5-2.0keV]	[erg s <sup>-1</sup> ]	kT [90% confidence]
RR 143a (NGC 2305)	8	120	5220±95	0.72	$1.2 \times 10^{-12}$	41.48	0.54 [0.52-0.56]
RR 242a (NGC 5090)	12	160	[5750±135]††	0.49	$1.1 \times 10^{-12}$	41.46	0.3 [0.25-0.37]; 2.7 [2.4-3.3]

NOTE.—  
† Best fit temperature(s) and 90% confidence limits assuming a MEKAL code. Low energy absorption is left free, but it is always consistent with the line of sight value. Abundance ratios are consistent with the solar value.  
†† Estimated excluding the central source.



TABLE 4  
LOG-BOOK OF WIDE FIELD IMAGING OBSERVATIONS.

(1)	(2)	(3)	(4)	(5)	(6)	(7)	(8)
RR 143	18-11-2001	V	N	$6 \times 500$	0.7	1.22	24.19
RR 143	17-11-2001	R	N	$6 \times 500$	0.7	1.22	24.53
RR 210	17-04-2002	V	Y	$6 \times 500$	0.8	1.18	24.12
RR 210	22-01-2002	R	Y	$6 \times 500$	0.7	1.03	24.48
RR 216	25-01-2002	V	Y	$6 \times 500$	0.7	1.02	24.15
RR 216	17-04-2002	R	Y	$6 \times 500$	0.7	1.08	24.44
RR 242	08-06-2004	V	Y	$6 \times 500$	0.9	1.13	24.06
RR 242	08-06-2004	R	Y	$6 \times 500$	0.9	1.05	24.41

<sup>1</sup>Pair

<sup>2</sup>Observing nights

<sup>3</sup>Filter

<sup>4</sup>Dither

<sup>5</sup>Exposure time [s]

<sup>6</sup>Seeing FWHM [arcsec]

<sup>7</sup>Airmass

<sup>8</sup>Zero Point

TABLE 5  
 FAINT CANDIDATE GROUP MEMBER POPULATION AROUND RR 143.

ID	$\alpha$	$\delta$	$m_R$ [mag]	V-R [mag]	n	$r_e$ [arcsec]	$\mu_0$ [mag/arcsec <sup>2</sup> ]	$\mu_e$ [mag/arcsec <sup>2</sup> ]
00006	06 47 20.3	-64 31 19	15.23	0.56	3.17	6.77	15.66	22.18
00028	06 49 06.8	-64 31 42	19.27	0.84	1.08	1.63	20.35	22.35
00035	06 47 51.2	-64 31 48	18.04	0.62	1.53	1.58	18.89	21.86
00751	06 47 49.6	-64 00 22	19.51	0.46	0.67	1.94	21.23	22.33
00754	06 46 07.3	-64 00 19	18.66	0.59	0.93	1.81	20.10	21.76
01042	06 47 10.1	-64 02 21	14.36	0.69	1.42	8.11	17.90	20.63
01127	06 50 53.6	-64 00 45	19.97	0.25	0.49	2.22	22.71	23.43
01326	06 50 59.0	-64 01 02	18.81	0.52	0.52	2.71	21.50	22.26
01908	06 50 13.3	-64 01 52	19.08	0.69	1.38	2.38	20.73	23.38
01991	06 47 26.8	-64 02 02	18.23	0.64	1.62	1.69	19.08	22.24
02314	06 50 05.5	-64 02 26	19.41	0.35	0.75	1.96	21.70	22.98
02457	06 47 36.9	-64 02 41	20.62	0.23	1.41	1.45	21.64	24.35
02483	06 46 37.6	-64 02 42	17.65	0.65	1.55	1.98	18.26	21.28
02668	06 49 06.7	-64 02 57	17.37	0.66	1.10	1.41	18.77	20.80
02862	06 46 08.8	-64 03 10	17.34	0.75	1.87	1.86	17.86	21.58
02883	06 46 31.9	-64 03 08	19.95	0.57	0.47	1.80	22.25	22.91
02940	06 46 57.0	-64 02 19	18.12	0.52	0.52	1.89	21.09	21.88
03090	06 49 01.7	-64 03 27	18.34	0.33	0.53	3.19	21.98	22.78
03218	06 46 32.4	-64 03 31	20.32	0.66	0.43	1.95	22.57	23.14
03285	06 48 25.9	-64 03 39	20.22	0.54	0.88	1.21	21.69	23.24
03859	06 48 03.7	-64 04 19	18.24	0.67	0.61	1.97	21.24	22.22
03964	06 47 28.4	-64 04 27	18.09	0.45	1.16	2.13	20.18	22.36
04070	06 49 18.4	-64 04 38	17.26	0.42	0.88	3.82	21.33	22.89
04264	06 46 53.5	-64 04 45	19.46	0.68	0.89	2.51	21.95	23.54
04342	06 50 41.1	-64 04 47	19.40	0.59	0.58	3.03	21.98	22.88
04431	06 50 55.7	-64 04 55	18.13	0.69	1.68	1.58	18.56	21.86
04693	06 50 56.2	-64 05 14	17.65	0.71	1.47	1.57	18.21	21.05
04748	06 48 36.4	-64 05 21	19.34	0.21	1.14	2.37	21.23	23.34
04874	06 48 24.7	-64 05 30	19.67	0.28	0.71	2.06	21.69	22.87
05014	06 46 46.7	-64 05 41	18.98	0.82	1.18	2.35	20.96	23.17
05046	06 46 25.9	-64 05 44	18.00	0.93	1.99	1.71	17.99	21.96
05363	06 48 41.3	-64 06 10	18.01	0.71	1.58	1.74	18.69	21.78
05526	06 48 00.8	-64 06 14	18.52	0.69	1.18	1.37	19.54	21.75
05757	06 46 14.0	-64 06 33	19.10	0.94	0.85	2.45	21.62	23.11
05769	06 48 22.9	-64 06 36	18.75	0.69	0.94	2.94	20.73	22.41
05889	06 47 57.8	-64 06 48	18.23	0.63	1.62	1.86	18.90	22.07
06038	06 46 22.1	-64 06 52	18.89	0.74	1.27	1.86	19.98	22.39
06070	06 48 27.0	-64 07 01	17.81	0.67	1.90	1.84	18.20	21.97
06152	06 50 12.4	-64 07 08	16.87	0.59	1.78	2.03	17.74	21.25
06304	06 48 27.5	-64 07 17	18.43	0.67	0.79	2.69	20.54	21.91
06315	06 49 01.8	-64 07 21	17.58	0.69	3.34	4.00	16.37	23.26
06459	06 46 51.5	-64 07 26	18.25	0.46	0.78	1.78	20.09	21.43
06608	06 47 51.8	-64 07 39	19.65	0.88	1.91	2.34	19.95	23.75
06644	06 48 13.9	-64 07 46	17.34	0.72	1.95	2.63	18.13	22.01
06858	06 47 45.1	-64 07 59	17.58	0.59	1.12	2.12	19.20	21.27
06959	06 47 18.5	-64 08 07	18.74	0.40	1.10	2.58	20.16	22.20
07232	06 47 51.1	-64 08 29	17.21	0.73	1.75	2.00	18.01	21.45
07559	06 50 41.4	-64 08 44	19.46	0.46	0.68	2.54	22.19	23.32
07742	06 46 58.1	-64 08 59	18.48	0.48	0.64	2.45	21.68	22.72
07870	06 46 26.2	-64 09 14	17.59	0.45	0.87	5.53	21.90	23.44
07998	06 50 16.9	-64 09 17	18.07	0.90	1.74	2.07	18.82	22.24
08023	06 49 35.3	-64 09 18	20.59	0.38	0.69	2.18	23.27	24.42
08451	06 47 37.5	-64 09 49	20.61	0.84	0.76	2.01	22.33	23.64
08730	06 47 42.1	-64 10 15	16.86	0.50	0.87	2.20	19.47	21.01
08875	06 51 02.4	-64 10 10	20.06	0.25	0.56	2.49	22.70	23.56
09030	06 46 04.0	-64 10 34	17.05	0.55	1.61	2.71	18.69	21.83
09192	06 47 53.3	-64 10 55	17.25	0.56	1.05	4.69	21.33	23.26

TABLE 5—*Continued*

ID	$\alpha$	$\delta$	$m_R$ [mag]	V-R [mag]	n	$r_e$ [arcsec]	$\mu_0$ [mag/arcsec <sup>2</sup> ]	$\mu_e$ [mag/arcsec <sup>2</sup> ]
09215	06 47 22.9	-64 10 44	18.89	0.47	0.97	2.40	21.15	22.90
09251	06 50 31.3	-64 10 43	19.63	0.32	1.14	3.63	22.40	24.53
09279	06 46 15.0	-64 10 40	19.55	0.39	0.48	2.13	22.51	23.19
10029	06 50 14.9	-64 11 34	18.96	0.89	1.09	2.47	20.79	22.81
10155	06 47 52.2	-64 11 51	17.85	0.52	0.81	2.31	20.39	21.80
10172	06 47 06.4	-64 11 52	17.48	0.62	2.52	2.34	17.11	22.23
10197	06 46 52.9	-64 11 50	18.07	0.67	1.65	2.09	18.92	22.15
10205	06 46 51.7	-64 11 46	21.07	0.24	0.24	4.13	25.01	25.19
10305	06 46 34.3	-64 12 01	17.49	0.63	0.90	3.36	19.89	21.49
10529	06 46 11.2	-64 12 09	19.40	0.31	0.42	2.51	23.08	23.63
10711	06 50 39.1	-64 12 18	18.81	0.85	1.45	1.67	19.52	22.31
10714	06 47 11.0	-64 12 27	19.51	0.53	0.62	2.10	22.38	23.37
10853	06 48 03.9	-64 12 41	16.76	0.65	2.06	2.53	17.19	21.31
11121	06 50 54.1	-64 12 44	20.25	0.74	2.42	2.47	20.24	25.15
11256	06 50 33.7	-64 12 57	18.29	0.20	0.72	2.78	21.78	23.00
11370	06 46 48.2	-64 13 07	18.78	0.69	0.68	2.00	21.37	22.49
11436	06 49 18.4	-64 13 15	18.37	0.53	0.87	4.29	22.51	24.04
12243	06 48 52.2	-64 14 07	20.40	0.27	0.68	1.98	22.94	24.06
12423	06 46 07.1	-64 14 17	19.17	0.45	0.65	1.87	21.80	22.85
12981	06 48 56.2	-64 15 09	17.73	0.45	0.70	3.21	21.15	22.32
13059	06 50 44.8	-64 14 58	19.27	0.98	1.07	1.82	20.95	22.91
13936	06 46 54.4	-64 16 23	16.68	0.44	2.05	1.22	16.03	20.12
14512	06 46 07.2	-64 16 59	19.96	0.63	0.48	2.03	22.37	23.06
14668	06 50 39.5	-64 17 11	20.11	0.54	0.48	2.12	22.25	22.94
15218	06 46 38.5	-64 17 57	19.30	0.39	0.87	2.75	22.18	23.72
15221	06 47 30.4	-64 18 01	17.20	0.59	1.11	2.77	19.71	21.76
15455	06 49 45.7	-64 17 54	17.46	0.48	1.07	0.67	17.74	19.72
15513	06 46 14.5	-64 18 21	17.93	0.69	2.10	2.21	18.34	22.56
15550	06 49 37.8	-64 18 38	14.95	0.53	1.43	11.32	19.45	22.21
15582	06 47 28.6	-64 18 23	19.86	0.24	0.55	2.97	22.89	23.73
15874	06 46 38.5	-64 18 48	19.23	0.32	0.71	2.43	22.48	23.68
16009	06 48 27.8	-64 18 59	19.50	0.58	1.58	3.74	21.98	25.05
16011	06 50 25.4	-64 18 56	20.00	0.31	0.70	2.08	22.93	24.10
16117	06 47 31.4	-64 19 08	17.58	0.65	0.93	2.27	19.41	21.07
16784	06 50 55.3	-64 19 60	18.65	0.47	0.53	2.71	22.26	23.07
16803	06 48 04.0	-64 20 08	17.64	0.51	0.73	2.09	20.05	21.28
16923	06 47 36.1	-64 20 15	18.69	0.57	0.69	2.52	21.01	22.16
17236	06 47 01.6	-64 20 37	20.30	0.37	0.60	2.11	22.24	23.18
17347	06 46 45.6	-64 20 48	19.65	0.71	0.82	1.87	21.28	22.72
17430	06 48 06.6	-64 20 55	19.69	0.39	0.90	1.52	21.67	23.27
17858	06 50 09.2	-64 18 37	17.01	0.42	1.12	1.97	19.16	21.24
17909	06 48 20.7	-64 21 31	19.21	0.83	1.05	1.71	21.10	23.02
18031	06 47 44.8	-64 21 40	19.06	0.43	0.96	1.66	20.92	22.66
18063	06 47 06.7	-64 21 43	18.42	0.63	2.09	1.80	18.36	22.55
18260	06 46 38.1	-64 21 53	19.26	0.69	0.69	1.96	21.79	22.94
18522	06 47 48.3	-64 22 15	19.50	0.32	0.77	2.56	22.48	23.80
18909	06 46 58.6	-64 22 41	18.64	0.55	0.90	2.42	21.41	23.00
18910	06 46 59.5	-64 22 45	17.53	0.70	2.51	3.91	17.61	22.72
19086	06 48 28.1	-64 22 57	18.43	0.51	1.12	2.67	20.81	22.90
20429	06 47 05.6	-64 24 54	18.14	0.57	0.96	4.13	20.98	22.71
20430	06 47 07.0	-64 24 44	16.41	0.64	2.42	3.93	17.04	21.94
20447	06 48 50.0	-64 24 42	19.63	0.41	0.67	3.83	24.00	25.11
20649	06 46 40.0	-64 24 55	19.94	0.34	0.65	2.48	23.09	24.15
20662	06 47 12.2	-64 25 01	17.22	0.87	1.37	1.78	18.04	20.66
20738	06 46 59.7	-64 25 07	17.06	0.67	1.86	1.87	17.57	21.25
21016	06 46 42.1	-64 25 22	17.48	0.48	1.09	1.84	19.49	21.49
21017	06 46 43.4	-64 25 26	17.92	0.45	0.76	2.73	20.97	22.27

TABLE 5—*Continued*

ID	$\alpha$	$\delta$	$m_R$ [mag]	V-R [mag]	n	$r_e$ [arcsec]	$\mu_0$ [mag/arcsec <sup>2</sup> ]	$\mu_e$ [mag/arcsec <sup>2</sup> ]
21044	06 49 37.7	-64 25 25	18.87	0.53	0.59	2.74	22.26	23.19
21086	06 47 29.8	-64 25 31	18.67	0.46	0.85	3.49	21.73	23.23
21093	06 49 11.0	-64 25 27	18.33	0.41	0.61	1.82	20.65	21.63
21166	06 47 00.3	-64 25 31	17.88	0.63	1.16	1.60	19.16	21.33
21187	06 49 59.1	-64 25 31	19.19	0.27	0.67	1.91	21.77	22.87
21324	06 50 35.7	-64 25 38	19.44	0.17	1.10	3.91	22.58	24.63
21357	06 48 48.2	-64 25 58	18.25	0.70	2.57	3.02	18.27	23.50
21426	06 46 57.9	-64 25 50	18.75	0.68	0.83	1.96	21.30	22.74
21465	06 47 33.0	-64 25 52	18.71	0.33	0.67	2.18	21.62	22.72
21533	06 49 04.1	-64 25 57	17.71	0.62	1.56	2.26	18.51	21.53
21872	06 50 01.9	-64 26 20	18.56	0.61	1.27	1.63	19.32	21.73
22375	06 49 31.8	-64 26 57	18.35	0.42	0.78	1.52	20.52	21.86
22457	06 48 09.6	-64 27 02	18.46	0.39	0.82	1.36	20.37	21.81
22627	06 47 07.3	-64 27 16	19.62	0.95	1.07	1.98	21.38	23.36
22752	06 48 13.8	-64 27 25	19.08	0.28	1.12	2.07	21.25	23.33
22971	06 48 24.3	-64 27 37	19.41	0.61	0.34	1.89	21.86	22.25
23417	06 47 33.8	-64 28 13	19.24	0.36	0.81	1.78	21.45	22.87
23734	06 49 18.3	-64 28 31	19.56	0.38	0.89	1.70	21.18	22.75
23758	06 46 27.9	-64 28 30	20.30	0.80	2.96	4.60	20.09	26.17
23796	06 50 31.9	-64 28 31	19.61	0.69	0.72	2.00	21.62	22.84
23823	06 49 03.3	-64 28 40	18.40	0.58	0.80	1.86	20.77	22.15
24029	06 46 33.0	-64 28 50	19.93	0.62	0.73	2.09	21.67	22.90
24043	06 46 28.0	-64 28 51	17.84	0.40	0.80	3.82	20.53	21.92
24188	06 50 20.6	-64 29 05	18.44	0.49	0.91	2.87	21.55	23.17
24246	06 47 07.5	-64 29 16	16.95	0.34	1.57	5.04	19.73	22.80
24333	06 48 40.5	-64 29 20	18.48	0.60	0.71	2.66	21.36	22.54
24388	06 47 45.9	-64 29 23	18.29	0.40	0.95	3.53	21.80	23.52
24473	06 50 57.9	-64 29 23	18.81	0.72	1.08	1.87	20.17	22.15
24606	06 46 19.4	-64 29 34	17.01	0.49	1.07	2.51	19.25	21.22
24607	06 49 34.2	-64 29 35	18.50	0.42	0.58	3.58	21.47	22.39
24732	06 47 26.1	-64 29 51	17.58	0.56	1.31	2.09	18.71	21.20
24743	06 47 47.9	-64 29 48	19.13	0.82	1.27	1.60	20.07	22.49
24778	06 47 32.1	-64 29 53	17.75	0.36	0.79	3.36	20.93	22.31
24811	06 46 26.6	-64 29 50	18.70	0.43	1.26	2.28	5.78	8.16
25304	06 47 52.6	-64 30 31	18.27	0.64	0.79	3.47	20.70	22.07
25310	06 50 56.9	-64 30 23	19.57	0.60	0.68	1.84	21.88	23.00
25500	06 47 55.6	-64 30 47	19.05	0.40	0.81	4.92	23.42	24.84

TABLE 6  
 FAINT CANDIDATE GROUP MEMBER POPULATION AROUND RR 210.

ID	$\alpha$	$\delta$	$m_R$ [mag]	V-R [mag]	n	$r_e$ [arcsec]	$\mu_0$ [mag/arcsec <sup>2</sup> ]	$\mu_e$ [mag/arcsec <sup>2</sup> ]
00129	12 07 09.0	-30 00 26	18.94	0.55	0.78	2.03	21.32	22.67
00232	12 05 47.2	-30 00 15	18.59	0.66	0.97	1.47	20.49	22.24
00371	12 05 52.4	-29 59 58	20.10	0.59	0.50	2.27	22.46	23.20
00554	12 06 46.1	-29 59 49	18.06	0.50	0.73	1.89	20.51	21.75
00568	12 06 43.5	-30 00 00	18.03	0.58	1.79	2.51	19.41	22.95
00654	12 05 50.2	-29 59 58	17.39	0.66	1.84	2.41	18.30	21.93
00889	12 06 58.9	-29 59 45	17.55	0.72	1.35	1.64	18.99	21.56
00910	12 07 41.4	-29 59 21	18.57	0.49	0.73	2.12	20.73	21.96
00967	12 07 25.3	-29 59 02	18.66	0.37	0.48	2.16	21.51	22.20
00988	12 06 58.2	-29 59 11	18.12	0.39	0.81	2.39	20.94	22.35
01257	12 07 13.0	-29 58 24	20.71	0.84	1.39	2.04	22.09	24.77
01264	12 06 59.5	-29 58 31	18.71	0.42	0.75	2.08	21.01	22.29
01475	12 06 46.2	-29 58 14	18.69	0.46	1.41	2.07	19.93	22.64
01668	12 07 16.6	-29 58 09	18.14	0.66	1.29	2.23	19.53	21.98
01701	12 05 51.4	-29 57 52	19.48	0.68	1.11	1.22	20.63	22.70
01840	12 06 59.9	-29 57 31	19.91	0.49	1.08	2.04	21.76	23.76
01941	12 05 56.8	-29 57 38	19.29	0.77	1.09	2.26	20.96	22.97
01967	12 07 21.1	-29 58 04	17.18	0.69	1.94	2.14	17.81	21.66
02053	12 05 39.7	-29 57 15	18.92	0.37	0.58	2.33	21.92	22.82
02146	12 05 52.6	-29 57 02	19.46	0.48	0.55	2.28	22.07	22.93
02265	12 07 16.4	-29 57 08	18.61	0.86	1.50	2.15	19.51	22.43
02612	12 07 33.0	-29 56 16	19.71	0.45	0.54	2.94	23.43	24.25
02724	12 06 23.1	-29 57 05	17.68	0.49	0.72	7.20	23.21	24.43
02924	12 07 47.8	-29 55 33	21.00	0.49	0.62	2.33	22.95	23.94
03105	12 05 42.5	-29 55 30	18.69	0.37	1.19	2.98	21.04	23.28
03106	12 06 34.9	-29 55 24	20.10	0.73	0.73	2.11	21.88	23.11
03409	12 07 13.7	-29 54 50	20.85	0.18	0.50	2.18	22.99	23.73
03532	12 06 15.2	-29 55 05	19.17	0.52	0.77	3.63	23.39	24.72
03533	12 06 31.3	-29 54 46	19.01	0.38	0.92	1.83	20.52	22.16
03549	12 07 47.8	-29 54 34	20.12	0.45	0.69	2.10	22.74	23.88
03693	12 06 36.7	-29 54 41	18.74	0.85	2.37	8.44	20.50	25.30
03747	12 06 38.1	-29 54 18	18.63	0.77	1.32	1.22	19.47	21.98
03791	12 06 48.7	-29 54 07	20.78	0.40	0.58	2.61	23.27	24.18
03865	12 06 01.0	-29 54 09	18.93	0.41	0.90	1.69	20.43	22.03
03871	12 07 42.0	-29 54 14	17.96	0.62	1.63	1.75	18.73	21.92
03970	12 07 28.6	-29 53 58	18.08	0.73	0.99	1.95	20.22	22.03
03974	12 07 31.9	-29 53 54	19.00	0.34	0.99	1.83	21.06	22.86
04072	12 07 44.1	-29 53 40	18.85	0.83	1.33	1.37	19.73	22.27
04421	12 07 24.4	-29 53 54	17.24	0.70	2.94	3.91	17.09	23.11
04493	12 06 54.5	-29 53 11	18.47	0.64	1.82	1.94	19.04	22.64
04504	12 06 07.0	-29 53 07	19.08	0.37	0.65	2.40	21.74	22.80
04512	12 07 09.8	-29 53 10	18.64	0.36	0.84	2.68	21.58	23.06
04614	12 07 03.4	-29 52 59	18.38	0.46	1.14	2.37	20.52	22.66
04665	12 07 34.1	-29 52 41	19.97	0.32	0.72	1.96	21.79	23.00
04682	12 07 40.9	-29 52 43	19.43	0.97	0.90	2.38	21.59	23.19
04789	12 05 57.6	-29 52 56	17.63	0.71	1.52	2.48	19.51	22.46
04807	12 06 19.5	-29 52 29	19.81	0.48	0.73	3.23	23.62	24.84
04935	12 05 38.6	-29 52 16	19.07	0.67	1.22	1.77	20.19	22.50
04951	12 06 44.1	-29 52 30	17.91	0.80	2.18	1.75	17.73	22.12
05034	12 07 38.2	-29 51 56	19.53	0.37	0.99	1.17	21.02	22.81
05135	12 05 33.6	-29 52 02	19.05	0.54	0.55	2.80	21.58	22.41
05166	12 07 25.4	-29 52 02	18.56	0.30	0.52	3.29	21.84	22.61
05265	12 05 59.4	-29 51 42	20.16	0.13	0.72	2.56	22.83	24.05
05365	12 06 44.4	-29 51 42	18.75	0.89	1.40	1.72	19.51	22.19
05778	12 07 37.5	-29 50 57	19.13	0.60	0.90	2.25	21.05	22.66
05987	12 06 03.4	-29 50 31	19.77	0.74	1.22	2.26	21.29	23.60
06080	12 05 52.6	-29 50 23	20.15	0.66	0.79	1.94	22.29	23.65

TABLE 6—*Continued*

ID	$\alpha$	$\delta$	$m_R$ [mag]	V-R [mag]	n	$r_e$ [arcsec]	$\mu_0$ [mag/arcsec <sup>2</sup> ]	$\mu_e$ [mag/arcsec <sup>2</sup> ]
06111	12 06 21.3	-29 50 17	18.77	0.47	0.77	2.20	20.89	22.21
06258	12 06 49.2	-29 50 06	19.69	0.69	0.85	1.89	21.79	23.28
06339	12 07 50.1	-29 50 09	16.87	0.62	1.45	1.70	17.89	20.70
06396	12 07 31.9	-29 49 56	19.08	0.33	0.66	2.49	22.37	23.45
06463	12 06 41.8	-29 49 41	20.05	0.29	0.39	3.48	22.91	23.40
06742	12 05 53.4	-29 49 23	19.99	0.44	0.47	3.31	23.93	24.59
06839	12 07 23.5	-29 49 05	19.79	0.76	1.01	1.96	21.35	23.19
06979	12 07 20.3	-29 48 56	19.65	0.29	0.52	2.09	22.15	22.94
07113	12 05 40.0	-29 48 46	18.12	0.51	1.21	1.43	19.10	21.38
07182	12 06 04.2	-29 48 38	20.03	0.65	1.98	3.45	20.82	24.76
07203	12 05 37.3	-29 48 26	20.17	0.45	0.41	3.54	23.32	23.86
07553	12 05 35.0	-29 48 16	17.24	0.57	0.99	2.19	19.25	21.06
07570	12 05 31.5	-29 47 57	19.10	0.60	1.08	1.92	20.25	22.24
07646	12 05 50.8	-29 47 59	19.09	0.38	0.95	3.24	22.04	23.76
07893	12 07 32.6	-29 47 37	19.73	0.29	0.67	2.39	22.54	23.65
08111	12 06 44.2	-29 47 23	18.71	0.67	0.54	2.29	21.75	22.56
08116	12 06 31.1	-29 51 33	14.24	0.58	1.39	7.85	19.05	21.71
08269	12 07 47.1	-29 47 00	19.43	0.93	1.42	2.29	20.86	23.60
08507	12 06 13.8	-29 46 37	18.66	0.91	1.11	1.49	19.81	21.87
08695	12 07 49.3	-29 46 25	18.17	0.77	0.96	2.28	20.54	22.27
08727	12 07 03.7	-29 46 20	19.12	0.75	0.93	1.60	20.57	22.24
08828	12 06 22.1	-29 46 00	19.46	0.48	0.48	2.45	22.05	22.75
09013	12 07 19.2	-29 46 05	17.05	0.50	1.01	2.31	19.61	21.44
09269	12 07 46.2	-29 45 53	17.26	0.91	2.38	3.31	18.02	22.83
09327	12 05 28.2	-29 45 15	18.46	0.79	1.14	1.83	19.50	21.62
09382	12 07 09.7	-29 45 15	19.34	0.85	0.83	3.21	21.59	23.04
09531	12 06 12.4	-29 44 58	19.38	0.15	0.55	1.93	21.91	22.76
09816	12 06 29.9	-29 44 21	19.11	0.62	0.90	2.05	20.82	22.42
10073	12 07 46.1	-29 44 12	17.74	0.87	1.40	1.69	18.98	21.67
10243	12 06 50.6	-29 43 51	17.88	0.53	1.18	2.35	19.71	21.93
10247	12 05 40.0	-29 43 39	19.91	0.42	0.72	2.03	21.87	23.08
10262	12 06 03.5	-29 44 17	17.05	0.79	2.00	2.65	17.71	21.71
10313	12 06 06.7	-29 43 41	18.99	0.53	0.73	2.28	20.96	22.21
10441	12 06 41.0	-29 43 39	18.00	0.34	1.25	2.13	19.85	22.21
10601	12 07 08.0	-29 43 24	17.77	0.44	0.83	2.66	21.07	22.52
10968	12 06 38.8	-29 42 43	17.43	0.67	1.70	1.56	17.99	21.32
11044	12 06 08.3	-29 42 23	19.86	0.31	1.11	2.38	22.17	24.23
11168	12 06 30.8	-29 42 34	18.96	0.61	0.46	3.89	22.54	23.18
11372	12 07 43.3	-29 43 11	17.59	0.50	0.83	6.97	22.21	23.66
11400	12 05 54.1	-29 41 57	18.18	0.58	0.58	2.91	21.07	21.97
11412	12 06 28.6	-29 41 55	18.16	0.68	1.00	1.81	19.27	21.10
11440	12 07 42.6	-29 41 57	18.32	0.83	1.35	2.48	19.98	22.57
11532	12 05 55.9	-29 42 16	16.75	0.63	2.35	3.75	17.60	22.34
11561	12 05 45.1	-29 41 45	18.92	0.62	0.78	1.93	21.38	22.72
11710	12 05 54.3	-29 41 13	19.99	0.37	0.65	1.98	22.06	23.13
11756	12 05 44.1	-29 41 30	16.48	0.62	1.45	2.31	18.45	21.24
11810	12 05 46.9	-29 41 14	17.69	0.56	1.26	1.70	19.06	21.44
11942	12 06 17.2	-29 41 00	18.38	0.64	1.21	1.93	20.24	22.51
12116	12 06 07.7	-29 40 44	18.12	0.54	0.85	1.88	20.64	22.13
12139	12 06 14.1	-29 40 46	18.46	0.65	1.82	2.02	19.06	22.66
12167	12 05 52.2	-29 40 37	18.83	0.69	0.68	2.51	22.17	23.30
12209	12 06 16.5	-29 40 14	20.05	0.54	0.90	1.40	21.81	23.42
12231	12 07 14.5	-29 40 23	19.46	0.52	1.34	3.58	21.47	24.02
12344	12 06 29.8	-29 40 07	20.68	0.25	0.51	2.04	22.80	23.57
12388	12 05 54.3	-29 40 01	19.22	0.40	0.88	2.48	21.49	23.04
12523	12 05 45.6	-29 40 51	16.27	0.62	2.12	2.91	17.35	21.60
12543	12 05 50.3	-29 39 58	18.91	0.49	0.79	2.58	21.82	23.18

TABLE 6—*Continued*

ID	$\alpha$	$\delta$	$m_R$ [mag]	V-R [mag]	n	$r_e$ [arcsec]	$\mu_0$ [mag/arcsec <sup>2</sup> ]	$\mu_e$ [mag/arcsec <sup>2</sup> ]
12686	12 07 21.7	-29 40 06	17.11	0.67	1.85	2.28	17.63	21.31
12828	12 05 59.2	-29 39 26	18.39	0.49	0.56	2.02	21.45	22.31
13000	12 05 46.3	-29 39 08	19.01	0.32	0.98	2.49	21.14	22.92
13089	12 06 15.3	-29 39 22	18.20	0.68	1.14	1.60	19.14	21.26
13169	12 06 06.0	-29 38 55	18.30	0.45	0.96	1.89	20.43	22.16
13231	12 05 34.0	-29 38 43	19.58	0.36	0.46	3.72	23.88	24.51
13285	12 06 31.4	-29 38 48	18.97	0.69	1.03	2.45	20.43	22.33
13373	12 06 55.0	-29 38 32	20.45	0.29	0.96	3.15	22.94	24.67
13417	12 06 16.0	-29 38 39	18.00	0.73	2.16	2.66	18.58	22.91
13481	12 06 46.6	-29 31 16	18.00	0.47	0.56	2.72	21.49	22.35
13493	12 06 50.3	-29 36 23	14.26	0.52	1.98	9.40	18.01	21.95
13578	12 07 03.2	-29 35 49	17.32	0.70	1.54	2.17	18.33	21.32
13651	12 05 59.0	-29 35 48	18.47	0.69	1.33	1.71	19.61	22.14
13676	12 07 28.9	-29 36 03	18.62	0.46	1.53	2.21	19.73	22.70
13744	12 06 16.1	-29 36 11	16.89	0.72	1.66	3.46	18.68	21.94
13813	12 06 29.4	-29 36 16	19.83	0.53	0.79	2.27	22.38	23.74
13833	12 06 16.4	-29 38 21	15.63	0.76	2.61	8.37	17.82	23.14
13879	12 07 48.2	-29 36 22	18.60	0.53	1.36	1.74	19.49	22.10
14043	12 06 15.2	-29 36 36	19.41	0.59	0.72	1.87	21.51	22.73
14191	12 06 59.1	-29 37 00	17.65	0.67	2.19	2.53	18.15	22.56
14298	12 06 20.4	-29 37 02	17.85	0.67	1.40	1.63	18.99	21.67
14371	12 05 30.9	-29 37 42	17.20	0.49	0.66	4.05	20.46	21.55
14386	12 06 19.4	-29 37 12	18.54	0.71	0.95	2.21	20.21	21.91
14460	12 06 30.3	-29 37 20	18.81	0.76	1.19	2.14	20.19	22.43
14705	12 06 00.9	-29 37 37	18.98	0.74	1.05	1.86	20.58	22.51
14731	12 06 35.4	-29 38 01	18.54	0.41	0.57	2.31	21.60	22.48
14880	12 05 54.4	-29 38 05	21.00	0.81	0.40	2.32	23.27	23.79
14888	12 06 17.3	-29 38 31	18.21	0.67	2.60	2.91	17.77	23.07
14950	12 05 59.7	-29 38 16	18.05	0.51	1.02	1.76	19.73	21.58
15020	12 05 35.7	-29 30 06	20.13	0.43	0.43	1.98	22.87	23.45
15115	12 05 43.4	-29 37 23	18.84	0.58	0.64	2.25	21.94	22.99
15176	12 06 24.2	-29 30 23	17.43	0.47	0.82	2.13	20.25	21.69
15704	12 07 48.5	-29 31 07	18.54	0.69	0.85	2.32	20.48	21.97
15730	12 05 56.3	-29 36 04	15.82	0.61	1.74	2.62	17.24	20.66
15863	12 06 06.3	-29 31 27	18.16	0.72	0.57	1.58	20.60	21.48
16036	12 07 03.9	-29 31 44	17.94	0.46	1.01	1.97	19.81	21.66
16130	12 06 07.4	-29 31 56	19.44	0.45	0.78	1.90	21.64	22.99
16347	12 07 39.3	-29 32 07	17.34	0.52	0.78	1.83	19.55	20.89
16463	12 07 42.2	-29 32 25	17.56	0.84	1.53	2.15	19.07	22.04
16595	12 07 23.6	-29 32 21	18.51	0.81	1.22	1.68	20.08	22.38
16960	12 06 38.8	-29 32 47	19.17	0.33	0.39	2.08	22.28	22.77
17023	12 05 54.8	-29 33 26	16.87	0.71	1.54	1.84	18.38	21.37
17074	12 05 58.5	-29 33 25	18.00	0.58	0.77	2.00	20.09	21.41
17127	12 06 09.5	-29 33 08	18.75	0.92	0.73	2.25	21.59	22.83
17346	12 07 34.9	-29 33 57	19.47	0.71	0.66	2.00	22.07	23.16
17416	12 06 34.3	-29 34 08	18.26	0.38	1.04	0.69	18.51	20.43
17464	12 05 50.5	-29 34 05	20.25	0.72	0.60	2.36	22.57	23.52
17675	12 06 09.3	-29 34 33	17.57	0.70	1.14	4.16	19.93	22.06
17787	12 05 51.0	-29 34 46	20.32	0.42	1.09	1.96	22.00	24.02
17795	12 06 09.4	-29 34 46	18.39	0.65	1.41	1.80	19.12	21.82
17798	12 06 32.2	-29 34 48	18.95	0.62	0.67	3.13	21.57	22.67
17809	12 06 14.3	-29 34 48	17.85	0.59	1.33	1.58	19.21	21.74
17860	12 07 27.5	-29 35 49	18.02	0.60	1.59	1.93	19.14	22.23
17953	12 06 25.2	-29 34 46	19.31	0.45	1.12	1.90	20.68	22.77
18009	12 06 34.8	-29 35 03	18.94	0.60	1.30	2.09	19.91	22.38
18064	12 07 28.0	-29 34 60	20.31	0.35	0.71	3.12	22.50	23.69
18245	12 06 54.4	-29 35 29	17.64	0.64	1.56	1.84	18.47	21.52

TABLE 6—*Continued*

ID	$\alpha$	$\delta$	$m_R$ [mag]	V-R [mag]	n	$r_e$ [arcsec]	$\mu_0$ [mag/arcsec <sup>2</sup> ]	$\mu_e$ [mag/arcsec <sup>2</sup> ]
18388	12 06 44.1	-29 35 44	18.47	0.61	0.92	2.53	20.61	22.25
18428	12 07 03.6	-29 35 42	18.45	0.52	0.90	2.36	20.72	22.32
18444	12 05 41.4	-29 35 37	20.00	0.21	0.52	2.47	23.12	23.89



TABLE 7  
 FAINT CANDIDATE GROUP MEMBER POPULATION AROUND RR 216.

ID	$\alpha$	$\delta$	$m_R$ [mag]	V-R [mag]	n	$r_e$ [arcsec]	$\mu_o$ [mag/arcsec <sup>2</sup> ]	$\mu_e$ [mag/arcsec <sup>2</sup> ]
00015	12 24 10.1	-39 59 31	18.47	0.47	0.74	1.87	20.43	21.70
00017	12 24 30.0	-39 59 28	16.20	0.59	1.03	6.54	20.37	22.25
00034	12 25 12.4	-39 59 50	19.29	0.49	0.65	1.88	21.49	22.56
00143	12 24 29.0	-39 29 21	17.19	1.03	1.17	1.64	18.83	21.02
00193	12 24 31.8	-39 29 33	18.06	0.72	1.72	1.74	18.59	21.98
00226	12 25 20.0	-39 29 36	20.03	0.60	1.27	5.74	23.21	25.62
00293	12 23 54.8	-39 29 41	18.75	0.76	0.71	3.03	21.44	22.63
00495	12 25 46.1	-39 29 54	18.81	0.28	1.21	1.95	20.20	22.47
00661	12 25 42.7	-39 30 12	19.42	0.43	1.44	2.04	20.82	23.59
01090	12 24 03.8	-39 30 35	19.07	0.58	0.69	1.91	20.96	22.10
01281	12 25 56.6	-39 30 54	18.32	0.71	1.49	1.51	18.81	21.69
01386	12 25 49.1	-39 31 02	18.75	0.82	0.85	2.65	21.16	22.64
01459	12 26 12.4	-39 31 08	17.90	0.74	1.59	1.86	18.74	21.84
01492	12 24 02.0	-39 31 06	19.16	0.46	0.87	1.41	20.91	22.46
01506	12 26 30.4	-39 31 07	19.39	0.58	0.91	2.03	21.13	22.75
01619	12 26 01.1	-39 31 21	18.57	0.92	1.45	2.57	19.97	22.76
01661	12 25 01.8	-39 31 20	18.41	0.75	1.33	1.68	19.10	21.65
01672	12 25 35.0	-39 31 20	18.57	0.65	1.04	1.78	20.21	22.11
01782	12 23 57.6	-39 31 26	19.11	0.45	1.06	1.98	20.86	22.82
01979	12 24 13.2	-39 31 49	17.97	0.57	0.48	5.05	21.21	21.90
01980	12 25 06.7	-39 31 46	16.64	0.64	1.56	1.71	17.60	20.63
02023	12 23 57.8	-39 31 46	17.62	0.51	0.98	2.91	20.51	22.30
02064	12 24 31.4	-39 31 49	19.67	0.60	0.70	2.58	21.68	22.84
02210	12 24 17.5	-39 32 00	20.52	0.87	0.34	2.06	23.46	23.85
02315	12 25 43.9	-39 32 29	17.64	0.68	3.34	4.73	16.77	23.66
02368	12 24 51.3	-39 32 23	16.60	0.49	1.00	5.50	20.89	22.70
02462	12 24 15.1	-39 32 21	17.98	0.66	1.08	1.46	19.39	21.38
02627	12 24 28.7	-39 32 33	20.60	0.47	0.72	2.17	22.68	23.88
02687	12 26 10.0	-39 32 39	18.91	0.90	1.13	1.70	19.96	22.07
02791	12 26 34.9	-39 32 46	19.51	1.02	1.15	2.02	21.24	23.39
02812	12 25 15.4	-39 32 54	17.65	0.74	1.30	1.06	18.19	20.67
03138	12 25 07.5	-39 33 11	19.06	0.71	0.69	2.40	21.23	22.38
03183	12 24 07.5	-39 33 12	18.10	0.78	1.50	1.68	18.84	21.75
03184	12 24 07.0	-39 33 16	20.34	0.52	1.24	2.39	21.72	24.06
03519	12 25 17.8	-39 33 46	17.26	0.51	1.02	5.22	21.35	23.22
03651	12 25 36.4	-39 33 53	17.90	0.79	2.05	2.09	18.29	22.38
03903	12 24 44.1	-39 34 08	18.53	0.64	0.90	1.89	20.82	22.41
04052	12 26 11.3	-39 34 47	14.57	0.60	1.07	10.78	20.12	22.09
04527	12 24 08.1	-39 34 54	17.95	0.87	1.30	2.16	19.37	21.84
04530	12 25 11.8	-39 35 07	15.84	0.44	0.88	5.92	20.28	21.85
04571	12 25 17.6	-39 35 05	17.37	0.81	2.09	3.07	18.42	22.60
04718	12 24 04.9	-39 35 16	17.12	0.73	0.67	4.53	20.97	22.08
04724	12 25 37.2	-39 35 11	17.79	0.76	1.82	1.77	18.20	21.80
04829	12 24 03.5	-39 35 15	20.16	0.50	0.58	2.55	22.47	23.38
04968	12 25 35.8	-39 35 28	18.77	0.62	1.96	2.11	18.98	22.88
05021	12 26 04.2	-39 35 31	18.26	0.76	1.51	1.40	18.84	21.77
05085	12 25 53.5	-39 35 35	19.59	0.61	0.62	2.66	21.80	22.79
05130	12 25 43.0	-39 35 39	18.77	0.51	1.24	2.08	20.69	23.03
05704	12 25 46.6	-39 36 22	18.95	0.52	0.84	1.73	21.20	22.66
06044	12 24 11.2	-39 36 44	18.38	0.70	1.11	1.76	19.73	21.78
06173	12 25 04.2	-39 36 30	16.04	0.61	2.25	2.38	16.40	20.93
06356	12 24 05.1	-39 37 16	15.69	0.76	2.60	2.95	15.80	21.10
06513	12 24 10.7	-39 37 21	19.40	0.54	0.66	1.99	21.36	22.44
06661	12 25 31.2	-39 37 37	17.53	0.77	2.16	2.09	17.55	21.89
06662	12 25 31.8	-39 37 52	17.96	0.39	1.22	3.09	20.53	22.83
06903	12 24 15.9	-39 37 50	18.16	0.54	1.33	1.77	19.61	22.14
06905	12 24 16.3	-39 38 02	16.81	0.68	2.13	2.14	17.02	21.30

TABLE 7—*Continued*

ID	$\alpha$	$\delta$	$m_R$ [mag]	V-R [mag]	n	$r_e$ [arcsec]	$\mu_0$ [mag/arcsec <sup>2</sup> ]	$\mu_e$ [mag/arcsec <sup>2</sup> ]
06937	12 23 54.9	-39 38 08	14.22	0.62	1.03	4.92	17.31	19.19
06976	12 24 11.6	-39 37 55	19.16	0.64	1.34	1.76	20.46	23.01
07080	12 25 16.1	-39 38 07	17.59	0.60	1.39	2.14	19.23	21.89
07630	12 24 18.3	-39 39 04	17.51	0.53	0.52	2.82	21.20	21.99
07648	12 25 19.0	-39 38 47	19.39	0.54	0.38	2.96	22.68	23.15
07705	12 25 21.3	-39 38 55	17.94	0.54	0.74	3.48	21.33	22.59
07784	12 25 15.4	-39 39 01	17.24	0.56	1.76	2.48	18.35	21.83
08792	12 24 22.5	-39 40 10	18.27	0.62	1.54	1.78	19.06	22.05
08843	12 25 53.7	-39 40 12	19.95	0.56	1.12	1.65	21.24	23.33
08963	12 24 10.7	-39 40 22	18.19	0.47	0.60	3.10	21.76	22.70
08966	12 24 21.9	-39 40 22	18.48	0.52	0.70	2.04	20.95	22.13
08992	12 23 59.9	-39 40 22	19.33	0.45	0.81	2.68	21.25	22.66
09657	12 26 13.9	-39 41 14	17.73	0.80	1.88	1.85	18.09	21.83
09665	12 25 20.9	-39 41 13	18.28	0.57	0.78	1.96	20.85	22.18
09684	12 24 39.8	-39 41 12	18.84	0.83	0.77	1.73	21.23	22.56
10148	12 25 14.3	-39 41 46	19.18	0.77	0.80	1.76	21.26	22.65
10584	12 25 42.2	-39 42 20	20.56	0.49	0.66	2.81	22.98	24.06
10605	12 25 23.9	-39 42 29	18.09	0.24	0.85	5.38	22.17	23.66
10619	12 25 27.4	-39 42 24	18.41	0.59	1.36	1.40	19.52	22.12
10886	12 26 27.3	-39 42 45	18.29	0.89	1.58	2.49	19.74	22.82
10904	12 24 54.3	-39 42 46	17.55	0.72	1.90	1.78	17.80	21.58
10920	12 26 12.7	-39 42 42	19.24	0.62	1.30	2.42	20.62	23.08
11539	12 24 52.3	-39 43 29	20.40	0.48	0.48	2.48	23.44	24.14
11612	12 25 39.4	-39 43 35	19.72	0.45	0.89	2.00	22.05	23.63
11736	12 24 55.5	-39 43 52	18.29	0.65	0.92	2.13	20.93	22.58
11798	12 24 48.9	-39 43 54	16.72	0.73	2.26	2.67	17.11	21.67
12152	12 25 32.8	-39 44 18	18.35	0.47	0.54	2.78	21.30	22.12
12209	12 25 37.0	-39 44 36	15.58	0.59	0.74	9.31	21.51	22.77
12359	12 25 26.8	-39 44 22	20.58	0.61	0.53	2.59	22.70	23.51
12412	12 24 54.4	-39 44 04	16.50	0.79	1.02	5.60	21.27	23.13
12620	12 24 41.1	-39 44 59	17.38	0.60	1.36	2.23	19.15	21.75
13025	12 25 08.0	-39 45 31	17.48	0.70	1.57	2.52	19.20	22.26
13075	12 25 37.2	-39 45 35	19.16	0.39	0.93	1.82	20.96	22.62
13275	12 25 52.6	-39 45 40	19.57	0.84	0.74	2.51	21.83	23.08
13385	12 25 08.9	-39 46 32	12.23	0.66	1.71	9.88	16.38	19.75
13646	12 25 25.5	-39 46 09	17.90	0.60	0.87	1.59	19.46	20.99
13712	12 24 18.5	-39 46 14	18.98	0.78	1.07	1.69	20.71	22.69
13937	12 24 07.3	-39 44 20	20.23	0.51	0.63	2.05	22.43	23.44
13978	12 25 22.2	-39 46 39	19.05	0.68	1.12	1.83	20.32	22.39
14011	12 25 00.3	-39 46 43	17.13	0.61	1.16	3.45	19.99	22.17
14077	12 26 33.3	-39 46 41	18.28	0.67	1.08	1.94	19.66	21.66
14194	12 25 36.6	-39 46 52	18.19	0.63	1.31	2.30	19.99	22.48
14268	12 24 09.1	-39 46 31	18.89	0.33	0.76	1.93	21.50	22.80
14445	12 26 34.2	-39 47 10	19.66	0.66	1.94	2.99	19.71	23.58
14557	12 25 21.3	-39 47 20	20.09	0.61	0.91	2.00	21.73	23.34
14618	12 23 53.7	-39 47 22	17.60	0.62	1.35	1.72	18.67	21.25
14785	12 25 59.7	-39 47 34	20.26	0.43	0.54	2.22	23.15	23.96
14882	12 24 15.6	-39 47 41	17.87	0.62	0.44	2.91	22.13	22.74
15464	12 24 34.4	-39 48 24	20.04	0.34	1.08	2.41	22.48	24.48
15509	12 24 53.3	-39 48 28	19.51	0.52	0.60	1.97	22.14	23.10
15688	12 24 17.9	-39 48 39	20.73	0.43	0.73	2.14	22.68	23.92
15689	12 24 21.4	-39 48 45	17.62	0.65	0.69	4.21	21.79	22.95
15690	12 24 21.7	-39 49 06	16.75	0.64	1.76	2.14	17.33	20.79
15819	12 24 06.9	-39 48 47	19.77	0.42	0.69	1.88	21.91	23.05
15885	12 24 24.6	-39 48 53	18.98	0.64	0.73	1.79	21.25	22.48
16231	12 23 54.8	-39 49 15	18.97	0.48	0.73	2.05	21.98	23.21
16334	12 26 21.8	-39 49 23	19.28	0.80	1.02	1.77	20.78	22.64

TABLE 7—*Continued*

ID	$\alpha$	$\delta$	$m_R$ [mag]	V-R [mag]	n	$r_e$ [arcsec]	$\mu_0$ [mag/arcsec <sup>2</sup> ]	$\mu_e$ [mag/arcsec <sup>2</sup> ]
16468	12 26 14.6	-39 49 34	18.39	0.62	1.20	1.90	19.81	22.06
16501	12 26 26.7	-39 49 35	19.51	0.97	1.30	2.82	21.76	24.22
16513	12 23 55.1	-39 49 32	20.86	0.81	0.95	1.35	22.41	24.13
16530	12 24 27.0	-39 49 37	19.58	0.46	0.55	1.96	22.35	23.21
16918	12 24 12.0	-39 50 04	19.76	0.84	0.67	1.85	21.95	23.05
16940	12 24 26.0	-39 50 07	18.05	0.57	1.00	2.56	20.84	22.66
17269	12 24 11.1	-39 50 28	20.01	0.30	0.76	1.85	22.47	23.78
17274	12 25 23.7	-39 50 40	15.45	0.63	1.72	3.07	17.35	20.73
17488	12 26 35.2	-39 50 49	17.79	0.69	0.93	3.33	21.21	22.88
17620	12 24 03.3	-39 50 53	17.80	0.49	0.73	1.80	20.61	21.83
17731	12 26 21.8	-39 51 04	19.67	0.45	0.41	5.83	23.93	24.46
17814	12 25 45.6	-39 51 09	19.56	0.56	0.62	1.84	21.95	22.94
18077	12 26 06.5	-39 51 35	17.90	0.39	0.40	9.11	24.14	24.66
18126	12 25 12.5	-39 51 33	19.14	0.47	0.76	2.26	21.04	22.33
18226	12 25 30.7	-39 51 41	19.76	0.39	0.69	2.37	22.46	23.61
18555	12 26 22.2	-39 52 18	16.38	0.74	3.22	3.28	15.64	22.28
18668	12 24 32.7	-39 52 12	19.66	0.81	0.66	1.95	22.01	23.09
18894	12 24 06.1	-39 52 34	18.84	0.43	0.66	6.12	23.88	24.95
19488	12 24 01.8	-39 53 12	18.96	0.40	0.71	2.14	21.80	23.00
19703	12 24 59.9	-39 53 39	19.55	0.40	0.66	1.86	22.06	23.13
19961	12 25 06.6	-39 53 57	19.88	0.59	0.67	2.38	21.94	23.04
20030	12 24 59.9	-39 54 02	18.84	0.63	0.59	2.17	21.58	22.50
20115	12 25 58.4	-39 54 08	19.28	0.63	0.90	2.03	21.12	22.72
20247	12 26 29.8	-39 54 16	18.91	0.88	0.77	2.09	21.12	22.44
20325	12 24 37.2	-39 54 28	17.42	0.43	1.12	4.66	20.71	22.80
20569	12 25 24.8	-39 54 38	20.15	0.89	1.14	1.47	20.95	23.08
20908	12 24 14.8	-39 55 03	18.18	0.55	0.69	3.84	22.27	23.42
21171	12 23 55.4	-39 55 20	18.25	0.58	0.71	2.58	20.77	21.96
21349	12 26 27.6	-39 55 33	18.86	0.76	0.93	2.19	20.79	22.45
21705	12 23 55.5	-39 55 58	19.62	0.47	0.65	1.94	21.55	22.62
21900	12 24 21.3	-39 56 14	17.94	0.64	0.97	3.36	20.01	21.77
22038	12 25 12.2	-39 56 26	18.42	0.49	0.69	2.00	20.66	21.81
22070	12 25 42.5	-39 56 31	17.86	0.63	1.31	1.65	18.93	21.42
22187	12 26 33.8	-39 56 38	17.39	0.72	1.86	1.95	17.74	21.42
22190	12 24 05.0	-39 57 18	16.64	0.64	2.77	2.34	15.91	21.58
22208	12 24 37.2	-39 56 31	19.93	0.82	0.27	1.92	22.45	22.68
22446	12 25 05.4	-39 57 01	18.65	0.46	0.67	2.61	21.42	22.53
22488	12 23 60.0	-39 57 01	17.33	0.58	1.02	2.15	19.39	21.26
22513	12 24 30.5	-39 56 60	19.86	0.68	0.37	8.88	24.89	25.34
22954	12 25 19.1	-39 57 37	19.05	0.94	1.78	1.57	19.23	22.75
23137	12 24 48.0	-39 57 50	19.12	0.97	0.73	2.16	21.50	22.73
23351	12 26 25.0	-39 58 05	20.28	0.70	0.48	2.17	23.17	23.87
23400	12 26 38.2	-39 58 07	18.82	0.92	1.37	1.58	19.31	21.92
23659	12 24 50.4	-39 58 34	17.77	0.63	1.05	4.43	20.36	22.28
23920	12 24 02.7	-39 58 50	16.56	0.51	0.94	2.47	19.24	20.92
23938	12 24 58.0	-39 58 50	20.21	0.55	1.06	1.82	21.62	23.56
23995	12 23 55.6	-39 58 58	16.37	0.58	0.84	4.21	20.31	21.79
24120	12 26 22.5	-39 59 06	16.20	0.57	0.85	2.64	19.43	20.93
24410	12 26 30.7	-39 59 23	19.83	0.89	0.67	2.35	21.86	22.97

TABLE 8  
 FAINT CANDIDATE GROUP MEMBER POPULATION AROUND RR 242.

ID	$\alpha$	$\delta$	$m_R$ [mag]	V-R [mag]	n	$r_e$ [arcsec]	$\mu_0$ [mag/arcsec <sup>2</sup> ]	$\mu_e$ [mag/arcsec <sup>2</sup> ]
00017	13 20 19.9	-43 55 57	17.03	0.69	3.05	3.58	16.44	22.72
00018	13 21 39.0	-43 55 54	17.85	0.77	2.46	1.90	16.98	21.97
00636	13 22 22.3	-43 27 10	18.63	0.43	1.30	2.30	20.89	23.36
00842	13 22 33.7	-43 26 06	20.32	0.49	0.61	1.99	22.43	23.41
00970	13 19 47.3	-43 27 32	19.54	0.64	0.71	1.84	21.59	22.79
01414	13 21 38.1	-43 26 20	16.50	0.63	1.96	1.68	16.45	20.35
02287	13 20 21.5	-43 28 23	20.46	0.47	0.60	1.89	21.98	22.93
02474	13 20 19.8	-43 27 48	16.66	0.62	2.99	2.67	15.81	21.95
02600	13 20 42.1	-43 28 40	20.55	0.62	1.04	3.16	21.95	23.85
02687	13 20 16.6	-43 27 19	14.02	0.60	0.83	13.02	20.66	22.10
02729	13 22 20.8	-43 28 49	16.08	0.68	1.66	3.01	17.94	21.20
03293	13 20 19.0	-43 29 33	18.15	0.39	1.93	2.06	18.21	22.04
05407	13 21 31.0	-43 30 51	18.21	0.67	1.09	2.00	20.04	22.05
05413	13 19 55.7	-43 30 52	17.76	0.72	0.96	1.61	19.19	20.93
05430	13 21 59.4	-43 30 48	19.89	0.54	1.84	2.93	20.63	24.27
05845	13 20 17.5	-43 31 11	20.55	0.50	1.36	5.13	22.98	25.58
05955	13 21 18.6	-43 31 15	17.90	0.59	1.51	1.53	18.13	21.05
06039	13 22 03.1	-43 31 16	18.12	0.57	0.88	1.47	20.01	21.58
06906	13 20 41.2	-43 31 56	19.37	0.48	0.81	3.50	22.54	23.95
07132	13 21 38.7	-43 32 09	17.67	0.44	0.68	3.67	21.62	22.74
08028	13 22 30.1	-43 32 41	19.15	0.65	0.84	1.52	21.31	22.79
08050	13 21 15.3	-43 32 51	17.99	0.51	0.77	2.75	20.12	21.43
08064	13 22 10.4	-43 32 56	17.85	0.64	1.21	5.45	21.79	24.06
08617	13 20 15.0	-43 33 15	20.02	0.53	0.48	1.88	22.05	22.75
08697	13 21 07.1	-43 33 16	20.48	0.53	0.67	1.99	21.87	22.98
08916	13 20 38.5	-43 33 29	18.72	0.44	0.81	3.49	21.05	22.45
09059	13 20 18.2	-43 34 17	14.91	0.58	1.01	5.75	19.61	21.46
09578	13 20 47.1	-43 34 02	17.22	0.54	0.72	4.71	20.97	22.17
10276	13 21 53.0	-43 34 30	18.54	0.71	1.69	1.47	18.56	21.89
10753	13 20 34.1	-43 34 53	17.62	0.64	0.86	2.08	19.80	21.33
10930	13 22 33.8	-43 35 01	17.11	0.64	2.53	2.21	16.49	21.64
10972	13 20 35.9	-43 35 01	20.15	0.59	0.68	3.22	23.57	24.69
11100	13 21 03.1	-43 35 12	17.29	0.68	1.13	3.84	20.67	22.77
11102	13 20 24.0	-43 35 08	20.41	0.35	0.58	2.27	23.41	24.32
11419	13 22 06.6	-43 35 28	16.56	0.84	3.08	3.64	16.13	22.47
12894	13 22 03.0	-43 36 25	20.29	0.93	0.51	3.03	22.59	23.36
13110	13 22 24.8	-43 36 33	18.11	0.55	1.20	1.75	19.47	21.73
13326	13 21 03.9	-43 36 58	16.15	0.60	1.42	8.70	20.06	22.78
13627	13 21 10.7	-43 37 07	16.69	0.62	1.73	2.86	18.00	21.41
13887	13 20 08.6	-43 37 14	19.71	0.44	0.63	3.40	22.11	23.12
14078	13 22 36.0	-43 37 22	20.51	0.51	0.91	2.24	22.06	23.68
14284	13 20 47.8	-43 37 36	17.13	0.59	1.34	1.41	17.84	20.41
15689	13 21 16.5	-43 38 53	17.73	0.74	1.38	3.02	20.38	23.02
16076	13 22 06.4	-43 39 08	19.82	0.60	0.54	2.94	22.09	22.92
16322	13 21 14.8	-43 39 19	20.63	0.24	0.59	2.47	23.50	24.43
16864	13 20 32.5	-43 39 47	17.24	0.63	0.94	2.87	20.07	21.75
18069	13 20 07.5	-43 40 36	19.40	0.63	1.27	2.24	21.17	23.58
18166	13 21 04.0	-43 40 50	19.28	0.42	1.03	1.72	21.02	22.91
18533	13 22 36.1	-43 41 06	18.58	0.56	0.89	2.37	21.37	22.95
18545	13 20 36.8	-43 40 46	18.07	0.53	1.46	5.19	21.18	24.00
18982	13 20 12.3	-43 41 40	15.86	0.71	3.15	2.83	14.87	21.35
20075	13 20 26.7	-43 42 28	16.33	0.55	1.51	5.70	19.93	22.85
20151	13 21 50.1	-43 42 15	19.64	0.47	1.42	2.06	21.52	24.25
20910	13 22 06.9	-43 42 48	19.84	0.48	0.57	2.43	22.49	23.37
20913	13 22 12.9	-43 42 47	19.38	0.90	1.46	1.86	20.31	23.14
21539	13 20 46.7	-43 43 20	18.93	0.72	1.15	1.98	20.09	22.24
21750	13 20 03.6	-43 43 29	18.76	0.49	0.69	2.08	21.56	22.70

TABLE 8—*Continued*

ID	$\alpha$	$\delta$	$m_R$ [mag]	V-R [mag]	n	$r_e$ [arcsec]	$\mu_0$ [mag/arcsec <sup>2</sup> ]	$\mu_e$ [mag/arcsec <sup>2</sup> ]
21838	13 20 20.4	-43 43 36	19.10	0.69	1.40	3.41	21.61	24.30
22150	13 21 32.3	-43 43 46	19.66	0.51	1.03	2.49	21.69	23.58
22454	13 21 40.5	-43 44 04	18.01	0.27	1.47	1.42	18.78	21.62
22678	13 22 27.8	-43 44 03	19.49	0.49	0.90	1.65	21.11	22.70
22809	13 20 02.3	-43 44 12	20.09	0.66	0.77	4.41	23.68	25.01
23181	13 21 29.9	-43 40 47	18.70	0.55	0.80	2.39	21.54	22.91
23290	13 21 42.2	-43 44 18	19.55	0.54	0.88	1.40	16.89	18.45
24352	13 21 14.8	-43 45 43	13.71	0.62	2.35	6.91	15.91	20.67
24968	13 20 12.8	-43 45 53	16.61	0.58	0.76	3.84	20.27	21.58
25266	13 20 34.1	-43 46 01	19.60	0.42	0.60	2.52	22.63	23.58
25510	13 22 30.5	-43 46 13	17.61	0.42	1.36	1.88	18.86	21.47
25575	13 19 44.2	-43 46 28	16.42	0.60	2.24	7.12	18.92	23.44
26321	13 20 53.5	-43 46 49	19.71	0.74	0.70	1.80	22.11	23.27
26778	13 19 54.9	-43 47 33	14.52	0.71	2.10	5.97	16.99	21.20
26874	13 21 46.9	-43 47 17	18.00	0.74	1.62	2.48	18.88	22.05
27628	13 21 28.6	-43 47 45	17.56	0.68	1.34	2.41	18.52	21.09
28535	13 20 38.0	-43 48 33	18.58	0.19	0.82	1.97	20.60	22.04
29229	13 20 06.4	-43 49 16	17.09	0.63	1.15	6.27	21.44	23.59
29391	13 22 09.8	-43 49 08	20.27	0.47	0.69	1.99	22.12	23.26
29430	13 21 23.1	-43 49 13	19.57	0.62	0.55	1.81	22.03	22.88
29780	13 20 04.3	-43 49 32	19.03	0.50	0.55	3.15	21.66	22.50
30223	13 19 47.1	-43 49 54	18.89	0.62	0.87	4.70	22.84	24.39
30287	13 20 37.4	-43 50 02	17.53	0.50	0.93	3.15	20.37	22.03
30578	13 21 48.3	-43 50 05	19.11	0.70	1.52	2.72	20.02	22.96
30790	13 19 59.6	-43 50 16	19.62	0.47	0.78	2.48	21.85	23.20
31206	13 21 11.3	-43 50 40	19.87	0.51	0.53	2.18	21.77	22.57
31496	13 22 36.4	-43 50 52	19.27	0.31	0.76	2.34	21.61	22.92
31744	13 19 59.7	-43 51 08	19.77	0.58	1.22	4.17	21.12	23.41
32672	13 21 53.9	-43 51 45	19.31	0.94	0.88	1.55	21.10	22.67
32890	13 20 43.4	-43 52 02	17.41	0.64	1.37	3.90	19.36	21.99
33526	13 22 12.0	-43 52 25	19.54	0.87	1.40	1.80	20.45	23.14
33553	13 22 10.8	-43 52 26	19.71	0.42	0.70	1.74	21.64	22.81
34453	13 21 14.8	-43 53 29	18.27	0.68	2.32	2.05	17.74	22.43
34710	13 19 45.3	-43 53 31	20.83	0.72	1.61	2.60	22.22	25.37
34877	13 22 01.6	-43 53 36	17.72	0.47	1.57	1.97	18.80	21.86
35172	13 20 00.5	-43 53 57	20.41	0.37	1.83	1.40	20.26	23.89
35824	13 21 38.1	-43 54 23	19.17	0.59	0.66	4.67	23.92	25.00
36209	13 20 33.3	-43 50 30	19.09	0.54	1.77	2.75	20.55	24.04
36679	13 20 37.5	-43 55 02	19.52	0.78	0.70	1.74	21.47	22.64
36865	13 22 28.6	-43 55 08	20.28	0.97	0.53	1.93	22.23	23.03
37278	13 20 39.7	-43 55 31	19.96	0.58	0.80	2.43	22.76	24.14
37730	13 21 39.8	-43 55 55	18.05	0.83	3.83	3.52	15.20	23.16
37952	13 22 05.7	-43 55 59	20.38	0.57	1.36	3.05	21.78	24.39
38051	13 21 31.0	-43 56 07	20.00	0.54	1.24	2.39	21.94	24.28
38663	13 21 32.4	-43 27 23	15.04	0.79	1.58	8.56	19.13	22.21

TABLE 9  
X-RAY SOURCES IN THE RR 143 FIELD

N	RA	DEC	Net <sup>†</sup> counts	Cnt <sup>†</sup> rate	flux <sup>†</sup> (erg s <sup>-1</sup> )	Instr
1	06 46 40.8	-64 16 02	26.71 ±6.18	0.0104	1.013168E-13	PN
2	06 47 16.0	-64 23 17	47.95 ±8.65	0.0519	7.104581E-13	PN
3	06 47 24.0	-64 23 32	78.73 ±10.07	0.0256	2.441722E-13	PN
4	06 47 27.4	-64 04 56	86.03 ±9.97	0.0355	3.905863E-13	PN
5	06 47 34.4	-64 18 34	22.64 ±6.15	0.0053	5.150544E-14	PN
6	06 47 40.0	-64 06 53	23.01 ±6.16	0.0073	7.321936E-14	PN
7	06 47 48.7	-64 19 56	25.63 ±5.95	0.0055	6.401829E-14	PN
8	06 47 55.9	-64 07 35	17.68 ±4.68	0.0056	4.716441E-14	PN
9	06 47 56.2	-64 17 15	76.23 ±9.37	0.0138	1.559576E-13	PN
10	06 48 03.8	-64 05 44	25.18 ±6.96	0.0124	1.051518E-13	PN
11	06 48 06.1	-64 09 26	225.91 ±16.56	0.0501	5.650568E-13	PN
12	06 48 07.3	-64 25 28	140.23 ±12.61	0.0393	4.409702E-13	PN
13	06 48 12.1	-64 07 55	36.15 ±7.37	0.0089	9.970893E-14	PN
14	06 48 17.1	-64 24 21	30.10 ±6.68	0.0076	8.745382E-14	PN
15	06 48 29.4	-64 20 50	18.03 ±5.14	0.0027	1.083030E-13	MOS
16 <sup>††</sup>	06 48 37.5	-64 16 23	1732.48 ±46.88	0.2422	2.084515E-12	PN
17	06 48 40.9	-64 15 43	238.34 ±19.60	0.0330	2.901262E-13	PN
18	06 48 42.9	-64 04 21	53.26 ±8.22	0.0179	2.009735E-13	PN
19	06 48 43.4	-64:17 01	54.07 ±11.29	0.0083	7.754885E-14	PN
20	06 48 50.1	-64 18 53	24.80 ±6.09	0.0038	4.573677E-14	PN
21 <sup>†††</sup>	06 48 50.6	-64 20 07	28.08 ±6.02	0.0039	1.758483E-13	MOS
22	06 48 51.6	-64 28 27	24.00 ±6.70	0.0082	8.467915E-14	PN
23	06 48 57.6	-64 21 18	104.25 ±11.40	0.0183	2.152999E-13	PN
24	06 49 01.9	-64 12 26	22.48 ±5.59	0.0036	3.057529E-14	PN
25	06 49 04.7	-64 10 01	50.88 ±8.68	0.0098	1.200122E-13	PN
26	06 49 11.8	-64 06 54	78.84 ±9.25	0.0211	2.692666E-13	PN
27	06 49 12.7	-64 21 30	12.97 ±3.69	0.0018	4.480486E-14	MOS
28	06 49 21.1	-64 08 12	15.06 ±4.30	0.0027	8.221321E-14	MOS
29	06 49 25.1	-64 22 43	28.51 ±6.16	0.0064	6.839695E-14	PN
30	06 49 30.7	-64 19 52	87.06 ±10.69	0.0161	1.638327E-13	PN
31	06 49 34.6	-64 22 32	19.37 ±5.18	0.0044	4.305953E-14	PN
32	06 49 46.9	-64 07 50	56.48 ±8.28	0.0167	2.240017E-13	PN
33	06 49 49.1	-64 17 52	22.52 ±5.89	0.0053	4.461954E-14	PN
34	06 49 51.9	-64:11 46	124.59 ±12.12	0.0317	4.061077E-13	PN
35	06 49 52.2	-64 13 58	23.34 ±6.67	0.0062	7.873910E-14	PN
36	06 49 56.8	-64 26 23	37.94 ±6.59	0.0141	1.800038E-13	PN
37	06 49 58.7	-64 20 09	63.02 ±8.68	0.0152	1.825993E-13	PN
38	06 49 59.6	-64 13 05	15.79 ±4.70	0.0037	3.716768E-14	PN
39	06 50 00.4	-64 18 24	29.74 ±7.14	0.0089	9.482519E-14	PN
40	06 50 06.7	-64 23 26	47.59 ±7.37	0.0148	1.280928E-13	PN

NOTE.—<sup>†</sup> In the full 0.5-10.0 keV band. Fluxes are derived for a power law spectrum with  $\Gamma = 1.7$  and galactic absorption.

<sup>††</sup> RR 143a

<sup>†††</sup> Companion RR 143b [NGC 2307]

TABLE 10  
X-RAY SOURCES IN THE RR 242 FIELD

N	RA	DEC	Net <sup>†</sup> counts	Cnt <sup>†</sup> rate	flux <sup>†</sup> (erg s <sup>-1</sup> )	Instr
1	13 20 00.0	-43 46 40	50.84 ±8.02	0.0102	3.082375E-13	MOS
2	13 20 12.2	-43 40 12	45.10 ±8.82	0.0082	1.227895E-13	PN
3	13 20 18.7	-43 33 56	79.76 ±10.21	0.0130	3.278396E-13	MOS
4	13 20 20.5	-43 51 24	38.20 ±8.09	0.0094	1.507757E-13	PN
5	13 20 22.6	-43 32 59	33.81 ±6.99	0.0056	2.065168E-13	MOS
6	13 20 29.8	-43 34 51	39.48 ±7.68	0.0066	7.311842E-14	PN
7	13 20 30.3	-43 41 44	30.38 ±7.96	0.0040	6.720174E-14	PN
8	13 20 40.3	-43 42 00	305.49 ±20.70	0.0323	3.203940E-13	PN
9	13 20 40.7	-43 49 20	19.66 ±5.55	0.0037	3.447273E-14	PN
10	13 20 40.9	-43 50 42	23.78 ±5.36	0.0034	1.416466E-13	MOS
11	13 20 43.0	-43 30 35	28.74 ±7.64	0.0065	8.991507E-14	PN
12	13 20 49.0	-43 52 24	116.28 ±12.17	0.0199	1.873789E-13	PN
13	13 20 50.1	-43 36 00	29.58 ±6.98	0.0037	3.102088E-14	PN
14	13 20 50.2	-43 51 20	159.05 ±13.93	0.0254	2.940479E-13	PN
15	13 20 51.1	-43 38 33	34.47 ±8.47	0.0036	4.542740E-14	PN
16	13 20 51.6	-43 40 27	33.53 ±8.53	0.0040	6.908156E-14	PN
17	13 20 56.0	-43 51 09	36.89 ±7.93	0.0056	6.668399E-14	PN
18	13 20 56.7	-43 34 11	28.52 ±7.56	0.0042	6.023459E-14	PN
19	13 21 03.4	-43 45 36	92.27 ±11.45	0.0088	1.019294E-13	PN
20	13 21 04.7	-43 37 27	53.40 ±9.48	0.0059	6.751434E-14	PN
21	13 21 05.4	-43 51 29	37.92 ±6.28	0.0050	1.852026E-13	MOS
22	13 21 07.7	-43 27 47	38.90 ±6.98	0.0121	1.949288E-13	PN
23	13 21 10.9	-43 37 08	52.11 ±8.77	0.0060	8.068702E-14	PN
24	13 21 11.0	-43 34 02	33.62 ±8.17	0.0048	4.076546E-14	PN
25 <sup>††</sup>	13 21 13.0	-43 42 17	2945.74 ±60.14	0.2549	2.977146E-12	PN
26	13 21 20.1	-43 32 16	26.76 ±7.40	0.0053	6.022906E-14	PN
27	13 21 21.8	-43 51 11	335.21 ±13.13	0.0724	6.975664E-13	PN
28	13 21 22.4	-43 33 48	22.08 ±5.71	0.0034	3.122640E-14	PN
29	13 21 23.9	-43 38 51	53.51 ±10.72	0.0057	7.059597E-14	PN
30	13 21 24.1	-43 38 36	207.54 ±17.29	0.0221	2.534329E-13	PN
31	13 21 28.7	-43 36 55	39.17 ±8.55	0.0049	5.430766E-14	PN
32	13 21 30.6	-43 49 13	50.61 ±12.26	0.0168	5.288067E-13	MOS
33	13 21 35.3	-43 48 11	56.77 ±9.91	0.0076	9.071488E-14	PN
34	13 21 40.3	-43 39 44	34.92 ±8.37	0.0043	5.560670E-14	PN
35	13 21 49.1	-43 36 12	51.48 ±8.66	0.0084	7.141674E-14	PN
36	13 21 50.4	-43 33 56	39.79 ±8.88	0.0089	1.612898E-13	PN
37	13 21 55.8	-43 37 19	42.51 ±8.14	0.0075	6.943100E-14	PN
38	13 22 00.6	-43 44 01	29.37 ±7.90	0.0051	5.243528E-14	PN
39	13 22 04.0	-43 43 52	45.88 ±9.36	0.0096	1.016975E-13	PN
40	13 22 24.2	-43 37 50	54.34 ±9.05	0.0159	1.351174E-13	PN
41	13 22 26.1	-43 35 17	110.34 ±12.09	0.0335	4.308571E-13	PN
42	13 22 33.3	-43 40 41	21.91 ±5.48	0.0061	5.127875E-14	PN
43	13 22 33.9	-43 38 51	45.95 ±8.58	0.0148	2.298704E-13	PN

NOTE.—<sup>†</sup> In the full 0.5-10.0 keV band. Fluxes are derived for a power law spectrum with  $\Gamma = 1.7$  and galactic absorption.

This figure "f1a.jpg" is available in "jpg" format from:

<http://arxiv.org/ps/astro-ph/0610116v1>



This figure "f1b.jpg" is available in "jpg" format from:

<http://arxiv.org/ps/astro-ph/0610116v1>

This figure "f7.jpg" is available in "jpg" format from:

<http://arxiv.org/ps/astro-ph/0610116v1>

This figure "f8.jpg" is available in "jpg" format from:

<http://arxiv.org/ps/astro-ph/0610116v1>

This figure "f9.jpg" is available in "jpg" format from:

<http://arxiv.org/ps/astro-ph/0610116v1>

This figure "f10.jpg" is available in "jpg" format from:

<http://arxiv.org/ps/astro-ph/0610116v1>

This figure "f11.jpg" is available in "jpg" format from:

<http://arxiv.org/ps/astro-ph/0610116v1>

This figure "f12.jpg" is available in "jpg" format from:

<http://arxiv.org/ps/astro-ph/0610116v1>

This figure "f13.jpg" is available in "jpg" format from:

<http://arxiv.org/ps/astro-ph/0610116v1>



This figure "f16.jpg" is available in "jpg" format from:

<http://arxiv.org/ps/astro-ph/0610116v1>

This figure "f17.jpg" is available in "jpg" format from:

<http://arxiv.org/ps/astro-ph/0610116v1>